https://doi.org/10.5194/egusphere-2023-2882
Preprint. Discussion started: 9 January 2024

Understanding the variation of Reflected Solar Radiation: A Latitude- and month-based Perspective

Ruixue Li[1], Bida Jian[1], Jiming Li[1], Deyu Wen[1], Lijie Zhang[1]

[1]Key Laboratory for Semi-Arid Climate Change of the Ministry of Education, College of Atmospheric Sciences, Lanzhou University, Lanzhou 730000, China

Correspondence to: Bida Jian (jianbd16@lzu.edu.cn) and Jiming Li (lijiming@lzu.edu.cn)

Abstract. The hemispheric symmetry of planetary albedo (PA) is crucial for the Earth's energy budget. However, our understanding of hemispheric albedo is still limited, particularly regarding its variations at finer spatial and temporal scales. Using 21 years of radiation data from CERES-EBAF, this study quantifies the contribution rates of different latitudes to the hemispheric reflected solar radiation and examines their seasonal variations. Statistical results show that the northern latitudinal zones of 0° to 40° contribute more reflected radiation than the corresponding southern latitudes, but the southern latitudinal zones of 50° to 90° compensate for this. From the equator to 40°, the latitudinal contribution to the hemisphere is high in autumn and winter and low in spring and summer; however, after 50°, the situation is reversed. And even during extreme cases, anomalies of the cloud component contribution play a dominant role in anomalies of the total reflected radiation contribution of the latitudinal zone in most latitudinal zones. Additionally, this study evaluates the performance of four radiation data (including: satellite and reanalysis data) in reproducing hemisphere albedo and its hemispheric symmetry compared to CERES-EBAF data. Under different symmetry criteria, the applicability of different datasets to hemispheric symmetry of PA studies varies. Note that the Cloud_cci AVHRR performs better in capturing hemispheric symmetry. However, none of these datasets can decompose the different components of reflected radiation well. These results contribute to advancing our understanding of hemispheric symmetry variations and compensation mechanisms, reducing the uncertainty of model simulations, and improving algorithms for different radiation datasets.

1 Introduction

Planetary albedo (PA) refers to the fraction of incoming solar radiation that is reflected back into space by the Earth's atmosphere, clouds, and surface. It plays a crucial role in regulating the Earth's

https://doi.org/10.5194/egusphere-2023-2882
Preprint. Discussion started: 9 January 2024

energy budget and global climate change (Wielicki et al., 2005; Stephens et al., 2015) by determining the amount of solar energy absorbed and distributed throughout the Earth-atmosphere system (Fu et al., 2000; Stephens et al., 2015). Studies have shown that a 5% change in PA can lead to an average global temperature change of approximately 1K (North et al., 1981), while a 0.01 change in PA can have a radiative forcing effect equivalent to doubling the amount of carbon dioxide in the atmosphere (Wielicki et al., 2005; Bender et al., 2006). Even small variations in PA can have significant implications for the development of Quaternary glaciations (Budyko, 1969). Therefore, it is crucial to quantify the basic statistical properties of PA, as well as understand the major principles and mechanisms governing its spatial-temporal changes and long-term trends at various scales, including annual, global, and even finer spatial-temporal scales (e.g., regional and monthly scales).

Nowadays, satellite data and model simulations have been widely utilized to investigate the climatology (George and Bjorn, 2021; Jönsson and Bender, 2022), spatial and temporal distribution characteristics (Loeb et al., 2007; Pang et al., 2022), and long-term trends of PA (Diamond et al., 2022; Stephens et al., 2022; Xiao et al., 2023) , as well as the contributions of different components (such as cloud, clear-sky atmosphere, and surface) to PA (Stephens et al., 2015; Jönsson and Bender, 2022). Long-term satellite records have indicated that the current PA maintains a relatively stable value of approximately 0.29 (Bender et al., 2006). Surprisingly, the annual mean reflected solar radiation in the Northern Hemisphere (NH) and Southern Hemisphere (SH) is nearly the same within measurement uncertainty, which is referred to as hemispheric symmetry (Loeb et al., 2009; Voigt et al., 2013; Stephens et al., 2015; Jönsson and Bender, 2022). However, although satellite observations have demonstrated the symmetry of hemispheric PA on inter-annual scales, state-of-the-art models still struggle to reproduce this essential feature due to inadequate representation of the underlying physical mechanisms for PA variation, particularly the poor modeling of compensatory effects of asymmetric clouds (Voigt et al., 2013; Stephens et al., 2015; Jönsson and Bender, 2022). As a result, mean hemispheric asymmetries persist in all-sky reflections from CMIP phase 3 to CMIP phase 6, with considerable spread among the General Circulation Models (GCMs) within each CMIP phase (Crueger et al., 2023). Additionally, models also fail to capture the observed decreasing trend in reflected shortwave radiation in both hemispheres. These limitations may stem from the inability of models to accurately simulate the components of PA and their respective contributions to the hemispheric symmetry of PA. In particular,

https://doi.org/10.5194/egusphere-2023-2882
Preprint. Discussion started: 9 January 2024

the annual mean reflected solar radiation at the hemispheric scale is comprised of the reflected radiation at finer spatial and temporal scales (such as regional and monthly scales). If models cannot accurately account for the contribution of each component to hemispheric albedo at finer temporal and spatial scales, it hinders our ability to identify potential regional maintenance or compensation mechanisms for hemispheric symmetry in PA. Furthermore, it introduces significant uncertainties in model simulations of PA at annual and hemispheric scales.

Indeed, the contributions of different latitudinal zones to PA vary significantly spatially and temporally due to variations in water vapor, aerosols, vegetation, and clouds (Hu and Stamnes, 1993; Loeb et al., 2007; Voigt et al., 2014; Letu et al., 2018; Li et al., 2018; Zhao et al., 2019; Yang et al., 2020). These changes in contribution are also influenced by local climate and large-scale circulation patterns. For example, as one of the important conjectures of the compensating mechanism for the hemispheric symmetry of PA (Voigt et al., 2013; Voigt et al., 2014; Stephens et al., 2015), the Intertropical Convergence Zone (ITCZ) plays a role in regulating cloudiness in the 10°S-10°N region, with its location and intensity varying seasonally (Hu et al., 2007). However, the presence of tropical clouds alone may not be the primary factor determining hemispheric albedo symmetry, as the maximum in tropical cloudiness is located in the NH along with higher contributions from the surface and clear-sky atmosphere of the NH (Jönsson and Bender, 2023). Instead, extra-tropical cloudiness, particularly in the SH, has been highlighted as an important factor in maintaining the symmetry of the annual mean hemispheric albedo (George and Bjorn, 2021; Rugenstein and Hakuba, 2023). Recent studies have emphasized the impact of the distinct land-sea distribution between hemispheres, which leads to enhanced oblique pressure activity at mid-latitudes in the SH (Hadas et al., 2023). This activity results in intensified storm tracks, increased cloud cover, and higher cloud albedo in the extratropical regions of the SH (George and Bjorn, 2021). These clouds effectively compensate for the asymmetries in clear-sky albedo between the NH and SH. The oblique pressure activity at mid-latitudes exhibits a distinct seasonal cycle, with winter storm tracks in the NH being almost three times longer than summer storm tracks, and seasonal meridional shifts occurring in the SH (Verlinden et al., 2011). It is important to note that the contributions of different latitudinal zones to hemispheric PA are not independent of each other. Changes in the contributions of different latitudinal zones can offset or amplify each other, resulting in an energy balance or imbalance between the two hemispheres. For example, anthropogenic emissions from Asia

https://doi.org/10.5194/egusphere-2023-2882
Preprint. Discussion started: 9 January 2024

not only enhance the local clear-sky atmospheric component of reflected radiation through direct aerosol effects but also significantly increase aerosol optical thickness in the northwestern Pacific through long-range transport. This, in turn, increases the amount of deep convective clouds due to the indirect effects of aerosols. The increased deep convective clouds can strengthen the storm track in the Pacific Ocean and increase the contribution of the cloud component (Wang et al., 2014). Therefore, a comprehensive analysis of the contributions of different components at different latitudes and their monthly variations would help to better understand the mechanism of hemispheric PA symmetry and reduce uncertainties in model simulations of PA.

Currently, satellite remote sensing products from the CERES mission, which are based on broad-band measurements, are invaluable for studying the energy balance of the Earth-atmosphere system (including changes in PA and hemispheric symmetry) and climate change (Loeb et al., 2018b). However, the relatively limited observation record of CERES (2000-present) makes it challenging to study hemispheric PA symmetry on longer time scales. In recent years, satellite radiometric products and reanalysis data with longer time coverage and finer spatial resolution have been released, and numerous assessments have been conducted by researchers (Cao et al., 2016; Schmeisser et al., 2018; Loeb et al., 2022). The Cloud_cci version 3 radiative flux dataset has been shown to be in good agreement with the CERES EBAF dataset at a global scale (Stengel et al., 2020). Zhao et al. (2022) systematically assessed the applicability and accuracy of the Cloud_cci radiative flux dataset over the Tibetan Plateau (TP) and found that although the AVHRR can better describe the spatial and temporal characteristics of top-of-atmosphere (TOA) radiative fluxes over the TP, it does not capture the long-term trend of cloud radiative effects well. Furthermore, the spatial and temporal distributions of global TOA reflected radiance from MERRA-2 and ERA5 have been compared with those from CERES (Lim et al., 2021), revealing that ERA5 shows better agreement with CERES than MERRA-2 in terms of seasonal fluxes. However, most of these assessments focus on the spatial and temporal reproducibility of these data in terms of global or regional radiative flux, while their performance in terms of hemispheric symmetry remains unknown. To understand the mechanisms maintaining hemispheric symmetry of PA on longer time scales, it is essential to systematically evaluate the usability of long-term radiative flux products in describing hemispheric differences in TOA reflected radiation and its components.

To enhance future investigations into the potential maintenance mechanisms of hemispheric

https://doi.org/10.5194/egusphere-2023-2882
Preprint. Discussion started: 9 January 2024

symmetry and to reduce uncertainties in model simulations, this study aims to utilize long-term satellite observations of radiative flux (e.g., CERES-EBAF ed4.2) to quantify the contributions of clear-sky atmospheric, surface, and cloud components to PA at finer spatial-temporal scales (e.g., regional and monthly scales). Additionally, we aim to analyze the spatial-temporal variability characteristics of these contributions. Furthermore, we will examine the variation of controlling factors in extreme anomaly years of reflective radiation contribution at different latitudes. In particular, we will comprehensively evaluate the reproducibility of inter-hemispheric reflected radiation and its components using various satellite and reanalyzed radiation datasets (including Cloud_cci AVHRR PM v3, ISCCP-FH, MERRA-2, and ERA5), with a focus on comparing them to CERES EBAF radiation products. The paper is structured as follows: Section 2 describes the data and methods used in the study; Section 3 presents the overall characterization, latitudinal zone distribution, seasonal variations, and driving factors of reflected radiative flux and its components in extreme anomaly years, as well as the assessment of different radiation datasets; and finally, Section 4 provides the conclusions.

2 Datasets and Methodology

2.1 Datasets

2.1.1 CERES and MODIS

The Terra and Aqua satellites of the NASA were launched into Earth orbit in 1999 and 2002, respectively. Here, we use the products from two instruments (Clouds and the Earth's Radiant Energy System (CERES) and Moderate-Resolution Imaging Spectroradiometer (MODIS)) flying on both the Terra and Aqua satellites to provide the monthly mean radiative flux, cloud properties and parameters of the underlying surface.

CERES utilizes satellite-based observations to measure the Earth's radiation budget and clouds (Wielicki et al., 1996; Loeb et al., 2018b). The CERES instrument is a scanning broadband radiometer that captures radiation data across three channels: the shortwave channel (0.3–5μm), the infrared window channel (8–12μm), and the total channel (0.3–200μm). In our study, we focus on filtered radiances within the shortwave spectrum (0.3–5μm). These radiances are first converted to unfiltered radiance (Loeb et al., 2001), and then transformed into TOA radiation flux using an empirical angular distribution model (Su et al., 2015). Instantaneous fluxes are converted to daily-averaged fluxes using sun-angle dependent

https://doi.org/10.5194/egusphere-2023-2882
Preprint. Discussion started: 9 January 2024

diurnal albedo models (Loeb et al., 2018b). Surface irradiances are independently calculated using aerosols, clouds, and thermodynamic properties derived from satellite observations and reanalysis products. These calculations are constrained by the TOA irradiance (Kato et al., 2013; Kato et al., 2018).

Based on the work of Stephens et al. (2015) and Jönsson and Bender (2022), we have selected the TOA and surface shortwave (SW) radiative fluxes from the CERES EBAF product to analyze the contributions of different components. The CERES EBAF product employs an objectively constrained algorithm (Loeb et al., 2009) that adjusts the TOA SW and longwave (LW) fluxes within their uncertainties to eliminate inconsistencies between the global mean net TOA fluxes and the heat storage in the Earth-atmosphere system (Johnson et al., 2016). We use CERES EBAF, edition 4.2 (Loeb et al., 2018b), for monthly mean radiative fluxes (incoming solar radiation, upwelling SW radiation at TOA, and both upwelling and downwelling SW radiation at the surface) during all-sky and clear-sky conditions between March 2001 and February 2022 (21 years) on a 1°× 1° resolution grid. Note that EBAF data prior to June 2002 are Terra records only. In order to minimize flux discontinuities between the Terra-only record and the Terra&Aqua record, the CERES EBAF Ed4.2 product applies regional climate adjustments to the Terra-only record.

The cloud property parameters (Cloud Fraction (CF), Cloud Visible Optical Depth (CVOD), Ice Water Path (IWP) and Liquid Water Path (LWP)) for this study from March 2001 to February 2022 are obtained from CERES_SSF1deg_Ed4.1. This product provides MODIS-derived cloud properties and auxiliary data from the observed transient footprint SSF Ed4A fluxes and clouds (Minnis et al., 2020). Daytime cloud properties are calculated from the MODIS visible and infrared channels. To keep consistency with the EBAF data and to minimize the errors due to the diurnal cycle of clouds, we have averaged the cloud properties data from the Terra and Aqua sources over their overlapped time period (2002.7-2022.2). However, since Aqua data are not available prior to July 2002, this may result in a little bit uncertainty. In addition, the Ice/snow Coverage (ISC) data of CERES SSF is also used in this study. Snow and ice daily coverage is derived from the NSIDC (National Snow and Ice Data Center) near real-time SSM/I-SSMIS EASE-Grid Daily Global Ice Concentration and Snow Extent products, which are then interpolated to monthly average products.

In addition to snow and ice coverage, local vegetation coverage is also one of the important factors to influence the change of land surface albedo (Betts, 2000; Sandholt et al., 2002). To indicate vegetation

https://doi.org/10.5194/egusphere-2023-2882
Preprint. Discussion started: 9 January 2024

greenness, the Normalized Difference Vegetation Index (NDVI) used in this study is the Terra MODIS NDVI 0.05-degree monthly product (MOD13C2 collection061), which is based on spatial and temporal averages of 16-day 1-kilometre NDVI. The NDVI is calculated as the ratio between TOA reflectance of a red band around 0.66μm and a near-infrared (NIR) band around 0.86μm. In general, higher values of NDVI indicate a higher density of green vegetation.

2.1.2 ISCCP-FH

The International Satellite Cloud Climatology Project (ISCCP) aims to provide global cloud coverage and cloud radiation characteristics (Schiffer and Rossow, 1983). As part of the ISCCP project, the ISCCP-FH radiation product contains SW radiation fluxes at five levels from the surface to the TOA (surface-680hPa-440hPa-100hPa-TOA) under all-sky, clear-sky and overcast-sky conditions as well as the diffuse and direct SW fluxes at the surface. ISCCP-FH is not produced using direct instrumental observations, but rather the ISCCP H series of data products that are derived from geostationary and polar-orbiting satellites (Young et al., 2018), adopting a complete radiative transfer model developed from the GISS GCM ModelE. As a third-generation product, ISCCP-H has become more advanced and has other improvements in radiation quality control, calibration, cloud detection (especially high clouds, thin clouds and polar clouds), cloud and surface properties retrievals (Zhang et al., 2023). The ISCCP-FH product consists of five sub-products, of which the PRF (surface-to-TOA flux profile) sub-product can provides 34 years of global radiative flux data from July 1983 to June 2017 with a spatial resolution of up to 1° and a temporal resolution of 3 hours. In order to be consistent with CERES EBAF data, this study uses the diurnal mean of monthly mean of 3-hour upward and downward SW radiative flux at the TOA and surface under all-sky and clear-sky conditions provided by the MPF (monthly average of PRF) sub-product.

2.1.3 AVHRR

The Cloud_cci project is part of the European Space Agency (ESA) Climate Change Initiative (CCI) program and aims to provide a long-term and consistent cloud property dataset (Hollmann et al., 2013). The Cloud_cci dataset is generated using the state-of-the-art retrieval system called "the Community Cloud retrieval for Climate" (CC4CL), which employs optimal estimation (OE) techniques and is applied to passive imaging sensors from current and past European and non-European satellite missions (Sus et

https://doi.org/10.5194/egusphere-2023-2882
Preprint. Discussion started: 9 January 2024

al., 2018). In our study, we have chosen the Cloud_cci AVHRR-PMv3 dataset, which offers comprehensive cloud and radiation flux properties on a global scale from 1982 to 2016. These properties are derived from measurements obtained by the Advanced Very High Resolution Radiometer (AVHRR) instrument onboard the afternoon (PM) satellite of the US National Oceanic and Atmospheric Administration's (NOAA) Polar Operational Environmental Satellite (POES) mission (Stengel et al., 2020). To account for the diurnal cycle of the solar zenith angle, all samples of the SW flux are rescaled and averaged to represent a 24-hour average for each pixel. This monthly average value is then determined (More details can be found in ESA Cloud_cci Algorithm Theoretical Baseline Document v6.2). It is important to note that the radiation broadband flux is determined by combining exported cloud characteristics with reanalysis data (Stengel et al., 2020). However, there are some discrepancies in this product for the years 1994 and 2000 due to the unavailability of AVHRR data. Therefore, data from these years are not utilized in our study. We use the monthly mean global 0.5° grid data (Level-3C) from Cloud_cci, which includes TOA and surface upward and downward SW radiative fluxes under both all-sky and clear-sky conditions. We interpolate this data to a 1° grid to maintain consistency with CERES.

2.1.4 Reanalysis datasets

The Modern-Era Retrospective Analysis for Research and Applications, version 2 (MERRA-2), is the latest atmospheric reanalysis of the modern satellite era produced by NASA's Global Modeling and Assimilation Office (GMAO) with version 5.12.4 of the Goddard Earth Observing System (GEOS) atmospheric data assimilation system (Gelaro et al., 2017). It is the first long-term global reanalysis to assimilate space-based observations of aerosols and represent their interactions with other physical processes in the climate system. MERRA-2 can provide long-term radiative and aerosol products with a spatial resolution of 0.5°×0.625° from 1980. Here, the radiative product from MERRA-2 is used for comparative assessment with CERES data, as well as the aerosol product and land surface product are used as the main influence factors of the clear-sky atmospheric component and surface component of the PA, respectively. M2TMNXRAD (or tavgM_2d_rad_Nx) monthly mean radiation flux data, including the incident and net downward SW radiative fluxes at the TOA and the surface under all-sky and clear-sky conditions, M2TMNXAER (or tavgM_2d_aer_Nx) 550nm total aerosol extinction optical depth (AOD) monthly data, and M2TMNXLND (or tavgM_2d_lnd_Nx) surface soil moisture (SM) monthly data from 2001 to 2021 are selected in this investigation.

https://doi.org/10.5194/egusphere-2023-2882
Preprint. Discussion started: 9 January 2024

ERA5 is the fifth-generation atmospheric reanalysis of the global climate from January 1940 to present by the European Centre for Medium-Range Weather Forecasts (ECMWF). ERA5 combines model data with observations from around the world to form a globally consistent dataset that replaces the previous ERA-Interim reanalysis. 4D-var data assimilation technique in the Integrated Forecasting System (IFS) Cycle 41r2 is used to ensure a significant improvement in prediction accuracy and computational efficiency (Jiang et al., 2019; Hersbach et al., 2020). It provides hourly estimates of a large number of atmospheric, land and oceanic climate variables with a spatial resolution of 0.25°×0.25° (Hersbach et al., 2020). The monthly average surface and TOA radiation budget products are used in this study. The total column water vapor (TCWV) data also come from ERA5.

In order to ensure data consistency, we resample the monthly mean diurnal averaged radiative fluxes and other meteorological parameters from MERRA-2 and ERA5 datasets to match the 1°×1° resolution of CERES.

It's important to note that for a more accurate comparison with CERES EBAF, we utilize the other radiative flux data mentioned above (SW radiative flux from ISCCP-FH, AVHRR, ERA5, and MERRA-2) for the overlapping time period of March 2001 to February 2016.

2.2 Methodology

2.2.1 Decomposition of planetary albedo contribution

To investigate the main drivers of the PA, we use the similar model as Stephens et al. (2015) to decompose the PA into the contributions of the surface and atmospheric components. Assuming that surface and atmospheric scattering have isotropy, planetary albedo R is defined as:

$$R = \frac{F_{\mathrm{TOA}}^{\uparrow}}{S} \tag{1}$$

Among them, the $F_{\mathrm{TOA}}^{\uparrow}$ is reflected SW (upwelling) flux at the TOA, S is the solar incoming (downwelling) flux. The transmittance T of the whole earth-atmosphere system is defined as:

$$T = \frac{F_{\mathrm{S}}^{\downarrow}}{S} \tag{2}$$

Where, $F_{\mathrm{S}}^{\downarrow}$ is the downwelling SW radiation at the surface. The surface albedo α is calculated as follows:

$$\alpha = \frac{F_{\mathrm{S}}^{\uparrow}}{F_{\mathrm{S}}^{\downarrow}} \tag{3}$$

Where $F_{\mathrm{S}}^{\uparrow}$ is the upwelling SW radiation at the surface. The term $F_{\mathrm{S}}^{\downarrow}$ can be expressed as:

https://doi.org/10.5194/egusphere-2023-2882
Preprint. Discussion started: 9 January 2024

$$F_S^{\downarrow} = tS + rF_S^{\uparrow} \tag{4}$$

Here, r and t represent atmospheric intrinsic reflectivity (that is, PA purely contributed by the atmosphere when surface albedo is assumed to be 0) and atmospheric transmittance, respectively. The r and t are calculated separately, so absorption and forward scattering are included in t. $F_{\mathrm{TOA}}^{\uparrow}$ can be represented as:

$$F_{\mathrm{TOA}}^{\uparrow} = rS + tF_S^{\uparrow} \tag{5}$$

By combining the above equations, R and T can be expressed by r, t and α:

$$R = r + \frac{\alpha t^2}{1 - r\alpha} \tag{6}$$

$$T = \frac{t}{1 - r\alpha} \tag{7}$$

According to the above equation, the values of r and t can be written:

$$r = R - t\alpha T \tag{8}$$

$$t = T\frac{1 - \alpha R}{1 - \alpha^2 T^2} \tag{9}$$

It can be seen that the planetary albedo R is composed of two parts: atmospheric contribution r and surface contribution $\frac{\alpha t^2}{1-r\alpha}$. These two parts are multiplied by the incoming solar radiation flux S respectively, and the respective contribution values of the atmosphere and the surface to the SW upwelling flux at the TOA ($F_{\mathrm{TOA}}^{\uparrow}$) can be obtained, namely $F_{\mathrm{atm}}^{\uparrow}$ and $F_{\mathrm{surf}}^{\uparrow}$ (unit: W m^{-2}).

$$F_{\mathrm{atm}}^{\uparrow} \equiv Sr \tag{10}$$

$$F_{\mathrm{surf}}^{\uparrow} \equiv S\frac{\alpha t^2}{1 - r\alpha} \tag{11}$$

Following Jönsson and Bender (2022), we further decompose the atmospheric component into clear-sky atmospheric and clouds contributions. The difference between the all-sky atmospheric contribution $F_{\mathrm{atm}}^{\uparrow}$ and the clear-sky atmospheric contribution $F_{\mathrm{atm,clear}}^{\uparrow}$ is considered as the cloud contribution $F_{\mathrm{cloud}}^{\uparrow}$. That is,

$$F_{\mathrm{TOA}}^{\uparrow} = F_{\mathrm{atm}}^{\uparrow} + F_{\mathrm{surf}}^{\uparrow} = F_{\mathrm{cloud}}^{\uparrow} + F_{\mathrm{atm,clear}}^{\uparrow} + F_{\mathrm{surf}}^{\uparrow} \tag{12}$$

$$F_{\mathrm{cloud}}^{\uparrow} = F_{\mathrm{atm}}^{\uparrow} - F_{\mathrm{atm,clear}}^{\uparrow} \tag{13}$$

2.2.2 Regional mean and contribution rate

The regional averaged TOA reflected SW flux F_k is spatially aggregated using the following calculation formula (Huang et al., 2012):

https://doi.org/10.5194/egusphere-2023-2882
Preprint. Discussion started: 9 January 2024

$$F_k = \frac{\sum_{i=1}^{N_k} W_{ki} \cdot \mathrm{F}_{ki}}{\sum_{i=1}^{N_k} W_{ki}} \tag{14}$$

Here, N_k is the number of grid samples in region k, and F_{ki} is the reflected SW flux corresponding to grid i in the region k. Here, $W_{ki} = \cos(\frac{\theta_i \cdot \pi}{180.0})$, where θ_i is the latitude of grid i. Regional averages for other variables are calculated according to the similar weighting equation.

In order to explore the contribution of different regions to the total reflected radiation at a hemispheric scale, the global latitude is divided into 18 latitude zones in the unit of 10°, that is, 90° N-80° N, 80° N-70° N, …, 70° S-80° S, 80° S-90° S. For example, the contribution rate of the cloud component C_{cloud} of each latitude zone to its hemispheric reflected solar radiation can be calculated by the following formula:

$$C_{\mathrm{cloud}} = \left(\frac{total\_latzone\_cloud}{total\_hem\_R}\right) \times 100\% \tag{15}$$

Here, $total\_latzone\_cloud$ and $total\_hem\_R$ are calculated from the molecular part of Eq. (14). Where $total\_latzone\_cloud$ refers to the sum of the cloud contribution of reflected solar radiation from all grid points in the given latitude zone, $total\_hem\_R$ is the sum of total reflected solar radiation from all grid points in the hemisphere in which the latitude zone is located (both taking into account the geodetic latitudinal weights of the different grids). The contribution of surface and clear-sky atmospheric components to hemispheric reflected radiation in different latitudinal zones can be derived by the similar method.

2.2.3 Time average

For the average contribution over time, we consider March to the following February as a complete year. Following the CERES EBAF Ed4.1 Data Quality Summary (2020), the monthly average data is weighted by the number of days in each month to obtain the annual average data (Wielicki et al., 1996; Loeb et al., 2009; Rugenstein and Hakuba, 2023). For example, the annual average value of TOA SW reflected radiation flux in a certain year is：

$$F_{Year} = \sum_{i=1}^{i=12} \frac{DAY_{mon}(i)}{DAY_{year}} F_{mon}(i) \tag{16}$$

where DAY_{year} is the total number of days in the given year, $DAY_{mon}(i)$ is the number of days in the current month, and F_{mon}(i) is the monthly averaged radiation flux. The annual average values of all variables are also obtained by this method.

https://doi.org/10.5194/egusphere-2023-2882
Preprint. Discussion started: 9 January 2024

2.2.4 CCHZ-DISO data evaluation system

To find out whether other radiation datasets can exhibit the similar hemispheric symmetry of PA, the CCHZ-DISO data evaluation system is also used. This method uses the Euclidean Distance between indices of simulation and observation (DISO) to evaluate the combined quality or overall performance of data from different models (Hu et al., 2019; Zhou et al., 2021; Hu et al., 2022). DISO has the advantage of quantifying the combined accuracy of different models compared to Taylor diagram (Kalmár et al., 2021). Moreover, the statistical indicators chosen for the Taylor diagram are fixed, whereas those in DISO can be taken and discarded according to the needs of the study (Hu et al., 2022). In particular, Taylor diagrams only provide statistical metrics on two-dimensional plots, DISO not only provides distances in three-dimensional space to quantify the comprehensive performance of a simulation model, but also allows a single statistical metric to capture different aspects of model performance (Hu et al., 2019).

In this paper, the difference of TOA reflected radiation flux between the NH and SH from CERES during 2001.3-2016.2 is taken as the observed data, while AVHRR, ISCCP, MERRE-2, ERA5 are considered as the model dataset. The correlation coefficient (CC), normalized absolute error (NAE) and normalized root mean square error (NRMSE) are used to construct the CCHZ-DISO 3D evaluation system. The smaller the value of DISO, the closer this model dataset is to the observed data, i.e., the better its composite performance.

$$\mathrm{CC} = \frac{\sum_{k=0}^{n}(a_i - \bar{a})(b_i - \bar{b})}{\sqrt{\sum_{k=0}^{n}(a_i - \bar{a})^2}\sqrt{\sum_{k=0}^{n}(b_i - \bar{b})^2}} \tag{17}$$

$$\mathrm{AE} = \frac{1}{n}\sum\nolimits_{k=0}^{n}(b_i - a_i) \tag{18}$$

$$\mathrm{RMSE} = \sqrt{\frac{1}{n}\sum\nolimits_{k=0}^{n}(b_i - a_i)^2} \tag{19}$$

$$DISO_i = \sqrt{(CC_i - CC_0)^2 + (NAE_i - NAE_0)^2 + (NRMSE_i - NRMSE_0)^2} \tag{20}$$

https://doi.org/10.5194/egusphere-2023-2882
Preprint. Discussion started: 9 January 2024

3 Results and discussion

3.1 Temporal variation of contribution of PA components in different latitudinal zones

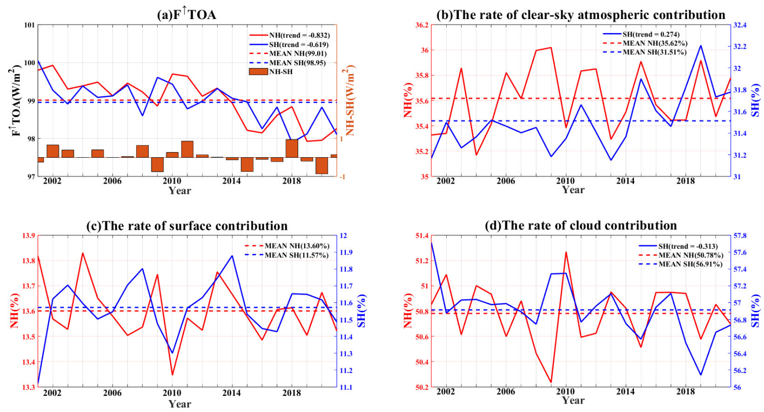

Figure 1: (a) The interannual variability of upwelling SW radiative flux at the TOA in the NH and SH from 2001 to 2021 (the left axis) and the annual mean difference between hemispheres (orange columns on the right axis). Interannual variation in the contribution rate of (b) the clear-sky atmospheric component, (c) the surface component, and (d) the cloud component to the SW upward radiative flux at the TOA in the NH (the left axis) and SH (the right axis); note that the scales of the two axes are not the same. The red line is for the NH, the blue line is for the SH, and the dashed line is the 21-year average. The trends labeled in the upper right corner passes the 99% significance test in units of W m^{-2} (10a)$^{-1}$ for (a) and % (10a)$^{-1}$ for (b)-(d). Unlabeled trends do not pass the test of significance.

Firstly, we examine the general characteristics of reflected radiation in the NH and SH on an annual average scale. Figure 1 illustrates the interannual variability of SW upwelling radiative flux at the TOA and the contribution rates of its three components in the NH and SH during the period of 2001-2021, based on CERES EBAF data. Supplementary materials (Fig. S1) provide further details on the interannual changes of reflected radiative flux by the three components. In a recent study, George and Bjorn (2021) argued that the symmetry of albedo cannot be established on an annual or sub-annual scale, but rather on larger spatial and temporal scales. In line with previous research (Stephens et al., 2015; Jönsson and Bender, 2022), our investigation demonstrates a clear symmetry in the total reflected radiation. This symmetry is evident in both the multi-year average of reflected radiation and the long-term trend of the annual average. The difference in the annual average total reflected radiant flux between

https://doi.org/10.5194/egusphere-2023-2882
Preprint. Discussion started: 9 January 2024

the hemispheres is less than 1 W m^{-2}, and the 21-year average difference approaches zero, indicating a nearly equal distribution of reflected SW radiation between the NH and SH. Figure S1d illustrates the cumulative year-to-year averaging of hemispheric differences in reflected radiation. It shows that the hemispheric differences in total reflected radiation and its components are decreasing or tending to stabilize over time, except for the clear-sky atmospheric component. The clear-sky atmospheric component exhibits a strong perturbation over time, which is closely tied to human activities, particularly the highly variable emissions of anthropogenic aerosols.

The reflected SW radiation at the TOA in both hemispheres exhibits a consistent decreasing trend (Trend_NH=-0.832 W m^{-2} (10a)$^{-1}$; Trend_SH=-0.619 W m^{-2} (10a)$^{-1}$), indicating simultaneous darkening of both hemispheres as observed from space. Moreover, the interannual variability of hemispheric differences is increasing, and the perturbations are intensifying. To investigate whether these trends in reflected radiation are linked to changes in incident radiation, we also present the interannual variations of incident solar radiation and PA (Fig. S2). The results indicate that the interannual variations of incident solar radiation at TOA in both hemispheres do not exhibit a clear trend, with the hemispheric difference following a stable multi-year cycle. However, PA in both hemispheres shows a consistent decreasing trend (Trend_NH=-2.4×10^{-3} (10a)$^{-1}$; Trend_SH=-1.8×10^{-3} (10a)$^{-1}$), suggesting a decrease in reflected solar radiation by the Earth as a whole and an increase in absorbed solar radiation. However, the same response in both hemispheres is driven by different component changes. The darkening of the SH can be primarily attributed to a decrease in reflected radiation from the cloud component (-0.661 W m^{-2} (10a)$^{-1}$) (Fig. S1c). In contrast, the reflected radiative fluxes by all three components in the NH show a decreasing trend, with the cloud component exhibiting the largest decrease (-0.448 W m^{-2} (10a)$^{-1}$), followed by the clear-sky atmospheric component (-0.219 W m^{-2} (10a)$^{-1}$), and the surface component showing the smallest decrease (-0.159 W m^{-2} (10a)$^{-1}$). However, there is no clear trend in the proportion of their contributions over the NH (Fig. 1). The decreasing trend of reflected radiation from the surface component in the NH mainly originates from changes in snowpack and sea ice at the poles, but its impact on the global average appears to be insignificant (Stephens et al., 2022). Additionally, the decreasing trend of reflected radiation in the NH can be attributed to reduced scattering of aerosol particles (Loeb et al., 2021a; Stephens et al., 2022) and a decrease in low cloud cover (Loeb et al., 2018a; Loeb et al., 2020). The decrease in low cloudiness may be linked to a shift in the Pacific Decadal Oscillation (PDO) phase

https://doi.org/10.5194/egusphere-2023-2882
Preprint. Discussion started: 9 January 2024

from negative to positive, resulting in warmer sea surface temperatures (SSTs) in parts of the eastern Pacific, which significantly reduces low cloud cover and reflected solar radiation (Andersen et al., 2022). To further investigate the inter-hemispheric differences in Earth's energy balance, we also calculate the trends of outgoing longwave radiation and net radiation at the TOA (figure not shown). A significant increasing trend of longwave radiation emitted to space is found in the NH (0.324 W m^{-2} $(10a)^{-1}$), while no significant trend is observed in the SH. Loeb et al. (2021b) noted that the increase in outgoing longwave radiation is primarily due to the increasing global surface temperature and changes in clouds, although it is partly compensated by the increase in water vapor and trace gases. However, the overall increase in outgoing longwave radiation does not outweigh the decrease in reflected shortwave radiation, resulting in a positive trend in the net radiative flux in both hemispheres (indicating that the Earth is absorbing more energy) (Raghuraman et al., 2021). This positive trend in the Earth's energy imbalance (EEI) will exacerbate global warming, sea-level rise, increased internal heating of the oceans, and melting of snow and sea ice (IPCC, 2013; Von Schuckmann et al., 2016; Loeb et al., 2021b). Indeed, a recent study based on long-term homogenized radiosonde data indicated that the atmosphere has become increasingly unstable in the NH during the period 1979-2020 (Chen and Dai, 2023).

In Fig. 1, the contributions of the three components to the PA exhibit varying degrees of hemispheric asymmetry. Among the three components, clouds contribute the most, accounting for over 50%, followed by the clear-sky atmosphere, and the surface with the least contribution. The cloud contribution in the SH is approximately 6.13% higher than that in the NH, which can be attributed to the presence of more abundant and brighter cloudiness in the SH. The clear-sky atmospheric contribution is 4.11% higher in the NH compared to the SH, possibly due to greater anthropogenic aerosol emissions resulting from human activities in the NH. The clear-sky atmospheric contribution rate in the SH shows an increasing trend of 0.274% per decade, which may be attributed to a decrease in the cloud component contribution of -0.313% per decade. This is because there is no clear trend in the reflected radiative flux by the clear-sky atmosphere in the SH, but there is a significant decrease in the cloud component (Fig. S1c). However, from a radiative flux perspective, the hemispheric asymmetry of the clear-sky atmosphere is decreasing (Fig. S1a), primarily influenced by the declining reflection of the clear-sky atmosphere in the NH, which is associated with the recent reduction of anthropogenic aerosols in eastern North America, Europe, and East Asia (Raghuraman et al., 2021; Quaas et al., 2022; Stephens et al., 2022). In comparison to the SH,

https://doi.org/10.5194/egusphere-2023-2882
Preprint. Discussion started: 9 January 2024

the NH exhibits a 2.03% higher surface contribution (Fig. 1c). Although the NH has a greater land distribution, the higher ice albedo in Antarctica partially compensates for the lack of land area in the SH, resulting in a less significant difference in surface contribution between the hemispheres.

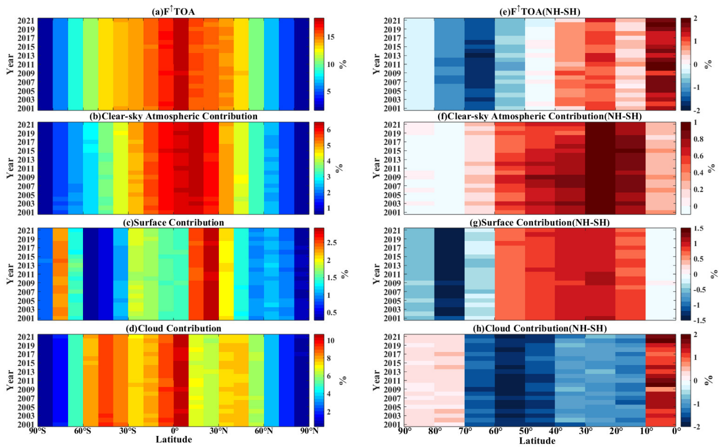

Figure 2: (a) Contribution of different latitudinal zones to hemispheric total reflected radiation at TOA from 2001 to 2021 and the corresponding components: (b) the clear-sky atmospheric component, (c) surface component and (d) cloud component. Contribution differences between the corresponding latitudinal zones of the two hemispheres (NH minus SH) are also given in (e), (f), (g) and (h).

Large-scale systems or certain compensatory mechanisms that may affect the hemispheric symmetry of PA do not directly operate on a hemispheric scale. Instead, they can compensate for hemispheric energy imbalances by influencing local or regional climates. For instance, oblique pressure activity, although primarily occurring at mid-latitudes, exerts a significant influence on cloud albedo, thereby strongly impacting global albedo (Hadas et al., 2023). While larger regional anomalies in reflected radiative flux may offset each other when spatially and temporally averaged to calculate global PA and its interannual variations, these anomalies play a crucial role in regional radiation budgets, subsequent climate change, and the identification of mechanisms that maintain or compensate for PA. Therefore, to gain further insight into the regional effects of these influencing mechanisms, we have divided the globe into 18 latitudinal zones in 10° increments. Figure 2 illustrates the contribution of each latitudinal zone to the total reflected radiation of its respective hemisphere, where (b)-(d) of Fig. 2 depict the contribution of the three components to the total reflected radiative energy of the hemisphere in each latitudinal zone.

https://doi.org/10.5194/egusphere-2023-2882
Preprint. Discussion started: 9 January 2024

In general, the interannual variation in the contribution rate of each latitude zone to the total hemispheric reflected radiation is small. However, there are still some relatively anomalous years, which will be discussed in detail in the next section (3.2). More energy is reflected from the 0°-40° latitude zones in the NH compared to the corresponding latitude zones in the SH (Fig. 2e). However, this imbalance is compensated by more reflection from the SH in the 50°-90° latitude zones. The dominance of the NH mainly arises from the clear-sky atmospheric contribution between 0°-70°, the surface contribution from 10°-60°, and the cloud contribution from the equator to 10°. In contrast, the strength of the SH at middle and high latitudes is derived from the surface contribution from 60°-90° and the cloud contribution from 10°-70°. Regarding clear-sky atmospheric contributions, the NH as a whole slightly exceeds the SH (except in the polar regions), possibly due to the higher presence of dust aerosols in the NH tropics and subtropics, as well as more sulfate pollution in the mid-latitudes (Diamond et al., 2022). Notably, the disparity in clear-sky atmospheric contributions between the two hemispheres is greatest at 20°-30° (around 1%), influenced by the combined effect of more dust and sulfate aerosols in the NH. There are significant hemispheric differences in surface contributions, with the NH exhibiting larger surface contributions concentrated in the 10°-60° latitude range, surpassing those in the SH. This discrepancy is expected due to the larger land area in the NH. Conversely, in the region from 60° to the poles, particularly from 70°-80°, the SH shows a greater surface contribution due to higher snow and ice coverage in the near-polar regions, resulting in more solar radiation reflection. However, over the Arctic, surface warming is occurring at a rate nearly four times faster than the global warming rate (Mika et al., 2022), leading to a continued decrease in Arctic ice cover. The SH also exhibits a significant contribution rate from clouds between 10° and 70°. This is not only attributed to lower contributions from the surface and clear-sky atmosphere but also to the prevalence of subtropical cloudiness and higher cloud albedo at mid-latitudes (Engström et al., 2017). The greater contribution of NH clouds near the equator may be due to the persistent presence of the Intertropical Convergence Zone (ITCZ) north of the equator in the eastern Pacific and Atlantic. This observation suggests that the SH heavily relies on extratropical clouds to compensate for clear-sky hemispheric asymmetries.

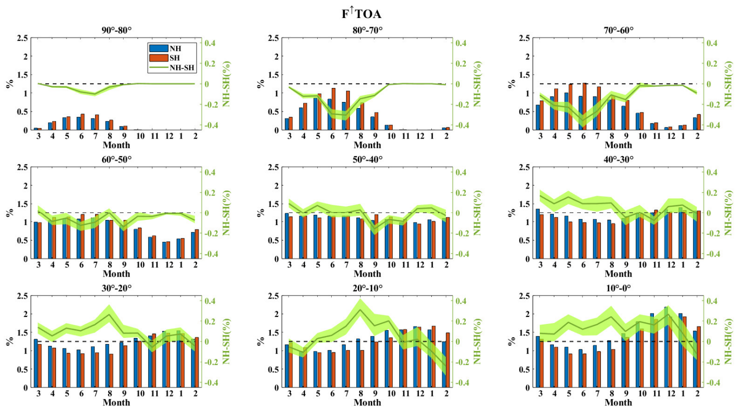

Figure 3: Monthly variation of the total reflected SW radiation contribution of different latitude zones to the total reflected SW radiation of their hemispheres and their hemispheric differences. The blue bars are for the NH, orange for the SH, corresponding to the left axis; the green line represents the inter-hemispheric difference, corresponding to the right axis, and the green shading indicates the difference spread in hemispheric difference for the corresponding month in that latitude zone during 2001-2021. The months are marked according to the NH, corresponding to the SH months of September, October, ..., January, February, …, and August.

The analysis presented above is based on the results of annual average reflected radiation. It is important to note that the symmetry of PA between hemispheres is a characteristic observed at interannual scales. However, certain natural and human activities that strongly influence albedo or compensate for hemispheric symmetry operate seasonally or even occur only in specific months of the year. These activities can have a significant impact on interannual scales, with their signals being more pronounced during particular seasons. We therefore hope to further clarify the variations of these mechanistic signals by resolving the reflected radiation and its components at finer temporal scale (e.g., monthly).

Figure 3 illustrates the monthly changes of contribution from different latitude zones to the total amount of reflected SW radiation and their contribution differences between two hemispheres. It is evident that the total reflected radiation from different latitude zones in both hemispheres exhibits noticeable monthly changes. From the equator to the 40° region, higher contributions are observed during autumn and winter, while lower contributions are seen during spring and summer. Additionally, in most months, the latitude zones in the NH have higher contributions compared to those in the SH. However, from the 50° to the polar region, the annual cycle of contribution rate reverses. Specifically, the contributions during spring and summer become more prominent in these regions. Notably, the latitude

https://doi.org/10.5194/egusphere-2023-2882
Preprint. Discussion started: 9 January 2024

zones in the SH consistently exhibit higher contributions to the entire hemisphere throughout the year compared to the corresponding latitude zones in the NH. This difference is particularly significant during June and July in the 60°-80° latitude range, primarily due to variations in contributions from the surface and cloud components (Fig. S4-S5). Overall, the annual cycle is primarily determined by seasonal variations in the contributions of the cloud component (Fig. S5) and the clear-sky atmospheric component (Fig. S3) at low and middle latitudes. Additionally, the surface component exerts a strong influence at high latitudes (Fig. S4). The reversal of the annual cycle of the latitudinal zone contribution of reflected radiation after 40° is mainly attributed to similar variability characteristics observed in incident solar radiation (Fig. S6).

From 10° to 60°, the surface contribution in the NH consistently exceeds that in the SH, likely due to the larger land area in the NH (Fig. S4). However, there is no clear monthly variation pattern for the interhemispheric differences in surface contributions within these latitudinal zones. At low latitudes, the surface contributions in both hemispheres exhibit similar monthly variations to those observed in the total reflected radiation contribution (Fig. 3). In the 0°-10° range, which is predominantly oceanic, the hemispheric difference in surface contributions is nearly negligible. From 60° to 90°, the dominant role of summer in the SH becomes more pronounced, with a greater contribution from the surface component compared to the cloud component at 70° S-90° S. However, in the NH, the cloud component still contributes the most at 60°-90°. Furthermore, in these high-latitude zones, there is no significant annual cycle in the hemispheric differences of incident solar radiation. Therefore, the hemispheric differences in surface contributions are primarily influenced by surface albedo (Fig. S7). These regions are located close to the poles and have extensive ice and snow cover. With global warming, ice and snow melting is occurring at a rapid pace, resulting in noticeable seasonal changes in ice and snow cover. Notably, at 70°-80°, the annual cycle pattern of the hemispheric difference in surface component contribution (Fig. S4) closely resembles that of surface albedo (Fig. S7), albeit with the latter exhibiting extremes 2-3 months later than the former. This discrepancy may arise from the fact that the contribution of the surface component is defined relative to the reflected radiation at the TOA, while surface albedo is influenced by cloud masking and modulation (Qu and Hall, 2005). Additionally, the surface contribution from the NH at 70°-80° peaks in May, one month earlier than in the SH, although both hemispheres experience their incident radiation peak in June (Fig. S6). This discrepancy is related to the distinct patterns of

https://doi.org/10.5194/egusphere-2023-2882
Preprint. Discussion started: 9 January 2024

monthly changes in surface albedo between the two hemispheres and the differential responses of polar snow and ice to global warming. The Arctic melt season is advancing and lengthening due to global warming and the Arctic amplification effect (Noël et al., 2015; Wang et al., 2018). From a hemispheric difference perspective, the annual cycle of total reflected radiation contribution primarily stems from the cloud component contribution in mid-low latitude regions and from surface and cloud contributions in high latitude zones, with the clear-sky atmospheric contribution exhibiting relatively weak variability. The interannual spread of the annual cycle of cloud component contribution is significant across all latitudinal zones, whereas the clear-sky atmosphere and surface contributions remain relatively stable. This indicates that the interannual variability of the seasonal radiation cycle in different latitudinal zones is predominantly driven by cloud contributions.

3.2 Contribution of different factors to latitudinal zones in extreme years

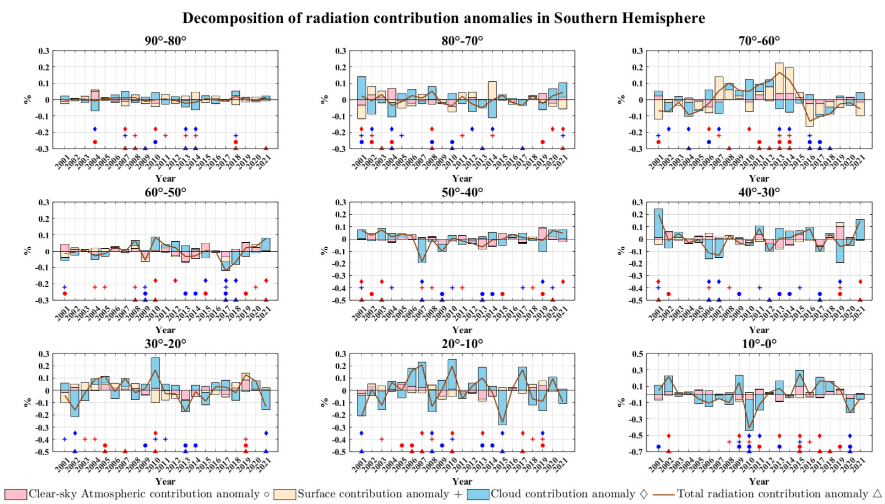

Figure 4: Anomaly time series of contribution rate of total reflected radiation and its three components of each latitude zone to total hemispheric reflected radiation in the SH during 2001 to 2021. The pink is the contribution anomaly of the clear-sky atmosphere, the yellow is the contribution anomaly of the surface, the blue is the contribution anomaly of the cloud, and the brown line represents the total contribution anomaly to the total hemispheric reflected radiation. The triangles labeled in the figure indicate that the contribution anomaly of total reflected radiation in this latitudinal zone for the year exceeds one of its standard deviations, i.e., it is an extreme value, with blue indicating extreme lows and red indicating extreme highs. Circles, plus signs, and diamonds indicate extreme values of clear-sky atmospheric contribution anomalies, surface contribution anomalies, and cloud contribution anomalies, respectively. Note that the vertical scale is different for different latitudinal zones.

https://doi.org/10.5194/egusphere-2023-2882
Preprint. Discussion started: 9 January 2024

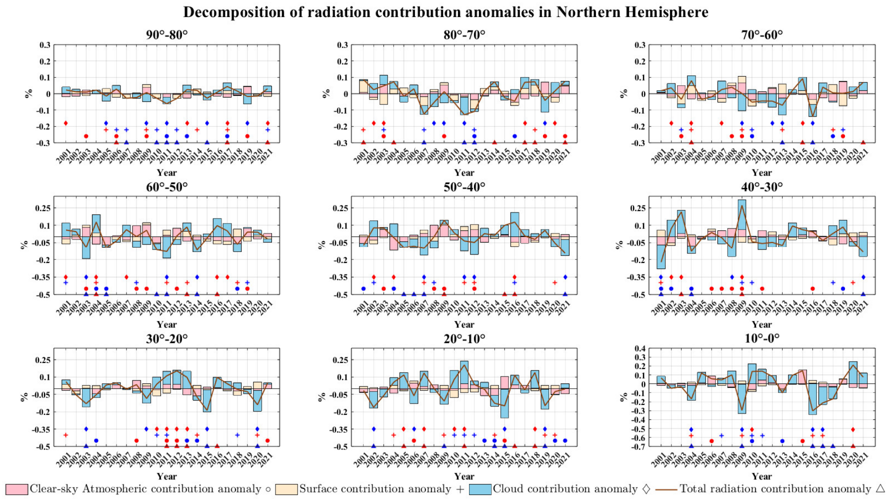

Figure 5: Same as Fig.4, but for the NH.

Different components play distinct roles in each latitudinal zone, and this section further explores which component dominates the variation of reflected radiation contribution under extreme conditions. It would be a valuable improvement if the model could capture the anomaly in contribution from different components across latitudinal zones during such extremes. Thus, we begin by decomposing the yearly contribution anomaly of total reflected radiation for each latitude zone into contribution anomalies of the three components. Subsequently, we identify extreme values of the total reflected radiation contribution anomaly and the three component contribution anomalies for each latitudinal zone by exceeding their respective one standard deviation (indicated in Fig. 4 and Fig. 5 using different symbols). Additionally, we label years with extreme anomalous values of total reflected radiation contribution anomaly as "extreme anomalous years" (represented by triangles in Fig. 4 and Fig. 5). Considering that variations in PA and its components are influenced by atmospheric and surface properties (Loeb et al., 2007; Voigt et al., 2014; Jian et al., 2018), we select surface-related factors: ISC, SM, NDVI; cloud-related factors: LWP, IWP, CVOD, CF; and clear-sky atmospheric-related factors: TCWV, AOD. To further correlate the anomalies contributed by different components in different latitudinal zones with changes in the control factors during extreme anomalous years, we calculate the proportion of anomalies in the different factors that fall outside their normal ranges (one standard deviation) (Fig. S8, S9). This proportion is obtained by calculating the annual mean anomaly of each factor in certain latitude zone minus its standard deviation and then dividing by the standard deviation. Importantly, it should be noted that the radiation

https://doi.org/10.5194/egusphere-2023-2882
Preprint. Discussion started: 9 January 2024

contributions from different latitudinal zones exhibit varying sensitivities to changes in different factors, resulting in different magnitudes of response. For instance, in the 10° S-20° S zone, snow formation is challenging and limited to high altitudes in the Andes Mountains (Saavedra et al., 2017). Therefore, changes in ISC in this latitudinal zone reflect changes in only a small part of the region and have little effect on the contribution of reflected radiation from the entire latitudinal zone.

Overall, the range of interannual variation in reflected radiation contribution is relatively large in the middle and low latitudes, while it remains more stable near the poles with minimal fluctuations. Previous studies have demonstrated that cloud variability dominates the variability of PA (Stephens et al., 2015; Seinfeld et al., 2016), and this conclusion holds true across different latitude zones. In most latitude zones in both hemispheres, especially in the tropics and subtropics, the radiative contribution variability is primarily influenced by the cloud component (Jönsson and Bender, 2022). This conclusion also applies to extreme cases. Globally, 87 % of extreme anomalous years are dominated by contribution anomalies from the cloud component, 10 % by the surface component, and 3 % by the clear-sky atmospheric component (Fig. S10). However, there is a slight difference between the NH and SH. In the SH, 18 % of extreme years are dominated by anomalies in the surface component contribution, compared to only 3 % in the NH. Among all events with extreme value occurrences caused by total radiative contribution anomalies or component contribution anomalies in both hemispheres (Fig. S11), 52 % do not exhibit extreme values in total radiative contribution due to the cancellation of contribution anomalies between different components. For example, in the 70° S-80° S latitude zone (Fig. 4), the cloud contribution in 2001 shows a positive anomaly and is the largest among the 21 years. However, since the contribution from the surface and clear-sky atmospheric components are negative anomalies, the total radiative contribution does not reach extreme levels.

In the latitude zones of 0°-30°, the variability of total radiation contribution is predominantly influenced by the anomalies in cloud component contribution, confirming previous studies that attribute tropical albedo variability primarily to cloud variability, especially associated with the El Niño-Southern Oscillation (ENSO) phenomenon (Loeb et al., 2007; Jönsson and Bender, 2022). For instance, in the 0-10° latitude zone of the SH, the extremely high anomaly in cloud contribution in 2015 can be attributed to the exceptionally strong and prolonged El Niño event that occurred in the east-central equatorial Pacific during 2015/2016 (Huang et al., 2016). The persistent anomalous ascending motions and large

https://doi.org/10.5194/egusphere-2023-2882
Preprint. Discussion started: 9 January 2024

amounts of water vapor in the east-central equatorial Pacific led to increased cloud formation (Avery et al., 2017; Lim et al., 2017), resulting in higher reflected radiation from the cloud components. Additionally, the significant positive anomaly in clear-sky atmospheric contribution can be linked to smoke pollution caused by extensive fires in equatorial Asia during September-October 2015 (Koplitz et al., 2016). It is observed that the combination of positive extreme anomalies in cloud state parameters (CVOD and CF) and clear-sky atmospheric parameters (TCWV and AOD) greatly influences the reflected radiation contribution (Fig. S8). Although there are large negative anomalies in SM due to extreme drought in the Amazon region (Jiménez-Muñoz et al., 2016), the impact of SM anomalies on the surface component contribution anomaly is limited in this primarily oceanic latitude zone. In 2010, the 20° S-30° S region was affected by a strong La Niña event, leading to anomalously heavy precipitation in Australia and South Africa and extreme positive cloud component contribution (Lim et al., 2016; Shikwambana et al., 2023). It is noteworthy that during this strong La Niña event, both the 0°-10° S and 10° S-20° S latitude zones exhibit dominant cloud contribution anomalies, but with opposite signs. A similar situation is observed during the 2015 El Niño event. This suggests the presence of some complementary mechanism between different latitudinal zones for radiative anomalies caused by such large and complex weather patterns. At 20° S-30° S, the extremely high reflected radiation contribution in 2019 is primarily contributed by the clear-sky atmosphere, which may be linked to the significant aerosol emissions from severe forest fires in Australia (Khaykin et al., 2020). This is supported by Fig. S8, which indicates that the anomaly of AOD for this latitude zone in 2019 exceeds 140 % of its standard deviation. In the 30° S-40° S latitude zone, although the total reflected radiation contribution is not extreme in 2019, the clear-sky atmospheric contribution exhibits a positive extreme anomaly that is counteracted by a negative contribution from the cloud component. This negative anomaly in cloud contribution may be associated with the combined effects of a positive Indian Ocean Dipole (IOD) and a central-Pacific El Niño on Australia during that period (Wang and Cai, 2020). At 70° S-90° S, while the surface component contributes the most to the reflected radiation (Fig. 2), it does not contribute as significantly to the variability of reflected radiation as the cloud component. Instead, in the 60°-70° latitude zone of the SH, the variation in reflected radiation contribution is primarily influenced by the surface component contribution, and its anomaly has an opposite effect to that of the cloud component anomaly. This indicates that clouds moderately mitigate the impact of sea ice changes on the total

https://doi.org/10.5194/egusphere-2023-2882
Preprint. Discussion started: 9 January 2024

reflected radiation contribution. The rapid expansion of Antarctic sea ice prior to 2014 results in anomalous ISC and a positive surface component contribution anomaly in this region during 2013-2014 (Riihelä et al., 2021).

The equatorial to 10° N region experiences strong negative anomalies in cloud state parameters (CF, CVOD, LWP) in 2009 (Fig. S9), leading to an extreme anomaly in the cloud component contribution. This is caused by a record-breaking warming in SST in the tropical North Atlantic starting in the summer of 2009. This warming is a typical response to ENSO and is influenced by the negative phase of the North Atlantic Oscillation (NAO) (Hu et al., 2011). In this region, 2016 is an extreme low year characterized by a negative anomaly in cloud component contribution due to the presence of a strong negative IOD and a weak La Niña (Lim and Hendon, 2017). This results in an abnormal decrease in cloudiness in the equatorial central Pacific region. In the mid-latitudes of the NH (Fig. 5), the contribution of the clear-sky atmosphere is more prominent due to the stronger influence of human activities in this region, with sulfate aerosols being the dominant aerosol component (Diamond et al., 2022). In 2019, the 30° N-40° N latitude zone exhibits a negative anomaly in the contribution of the clear-sky atmospheric component, primarily due to a significant reduction in atmospheric aerosols over much of east-central China. This reduction is a result of emission reductions implemented during the COVID-19 outbreak as part of epidemic control measures in China (Letu et al., 2023). In the Arctic, the contribution of the surface component is minimal (Fig. 2), but it becomes the secondary dominant component in the variation of the total radiative contribution after the cloud component. However, overall, the total radiative contribution anomaly in the Arctic is still primarily influenced by the anomaly in the cloud component contribution.

In conclusion, whether in low or high latitudes, and whether considering long-term perturbations or extreme events, the impact of cloud variability on changes in the contribution of reflected radiation in different latitudinal zones cannot be ignored. Therefore, accurate modeling of the cloud component is crucial. It has been demonstrated that climate projections are sensitive to different parameterization schemes for cloud radiation (Li and Le Treut, 1992; Li et al., 2022). If the cloud parameterization scheme is not well-refined, the model will struggle to accurately simulate reflected radiation at the TOA, making it challenging to explore the potential mechanisms behind the hemispheric symmetry of the PA.

https://doi.org/10.5194/egusphere-2023-2882
Preprint. Discussion started: 9 January 2024

3.3 Performance of different datasets on hemispheric asymmetry

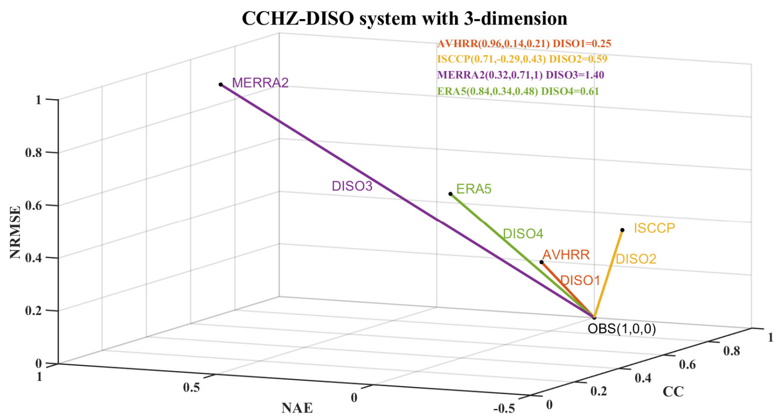

Figure 6: CCHZ-DISO system with 3-dimension. The coordinate axis consists of three statistical indicators, correlation coefficient (CC) for x-axis, normalized absolute error (NAE) for y-axis, and normalized root mean square error (NRMSE) for z-axis. OBS indicates observations, here referred to as CERES EBAF.

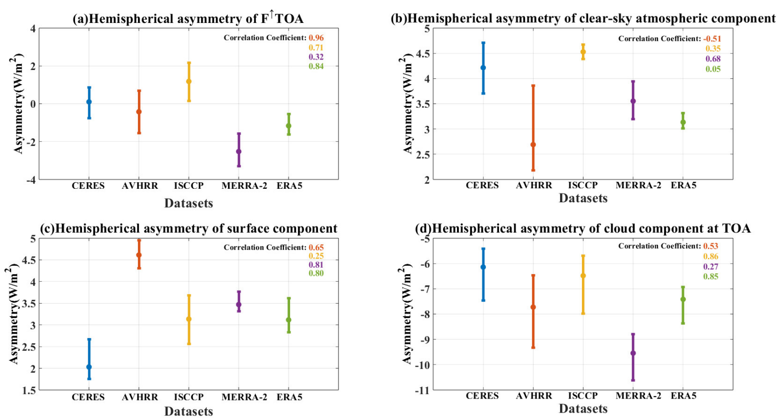

Figure 7: Multi-year averages of hemispheric differences in (a) TOA SW upwelling radiation flux and its (b) clear-sky atmospheric, (c) surface, and (d) cloud components for the five datasets from Mar./2001-Feb./2016, with the maximum annual average difference for the dataset at the top of the error bars and the minimum at the bottom of the error bars. Blue for CERES EBAF, orange for Cloud_cci AVHRR, yellow for ISCCP, purple for MERRA-2, and green for ERA5. The numbers in the upper right corner are the correlation coefficients of time series for hemispheric differences of the different datasets with CERES EBAF.

As mentioned earlier, AVHRR, ISCCP, MERRA-2, and ERA5 provide longer-term TOA reflected SW flux data compared to CERES EBAF. If these datasets can reproduce the observed hemispheric symmetry of reflected radiation captured by CERES, it would greatly assist in identifying the underlying

https://doi.org/10.5194/egusphere-2023-2882
Preprint. Discussion started: 9 January 2024

mechanism responsible for the hemispheric symmetry of PA using data spanning longer time periods. Therefore, in order to comprehensively assess the performance of each dataset, Figure 6 presents three-dimensional results based on CERES EBAF data using the CCHZ-DISO data evaluation system. Different assessment metrics yield different results (Table S1), highlighting the importance of selecting appropriate assessment metrics based on the specific research needs to obtain the most suitable dataset. In general, the results indicate that AVHRR has the closest DISO value to CERES (DISO1=0.25) and exhibits the best performance in terms of hemispheric symmetry. It is followed by ISCCP (DISO2=0.59) and ERA5 (DISO4=0.61), while MERRA-2 performs the worst (DISO3=1.40). It should be noted that the inclusion of spatial correlation coefficient in the DISO system did not significantly alter the results (Table S1c), so the three recommended metrics (CC, NAE, and NRMSE) are still used. Additionally, AVHRR demonstrates the highest correlation coefficient (0.96) with CERES for the time series of hemispheric differences in total reflected radiation, and their multi-year averages are the closest (Fig. 7a). Lim et al. (2021) have shown that ERA5 exhibits good agreement with CERES in simulating the inter-annual variation of global TOA SW reflected radiation. Moreover, ERA5 and ISCCP display good correlations with CERES (0.84 and 0.71, respectively), despite slight underestimation and overestimation of NH reflected radiation. Among all the datasets, MERRA-2 exhibits the poorest performance in terms of hemispheric symmetry, which may be primarily influenced by cloud cover bias (Lim et al., 2021).

To better investigate the performance of hemispheric symmetry in the reflected solar radiation across different datasets, Figure S12 illustrates the variation in multi-year average hemispheric differences of the reflected radiation and its components over time. We aim to determine the timescale suitable for studying the hemispheric symmetry of PA using these datasets. Since previous studies lacked a clear definition of PA's hemispheric symmetry, we will discuss this issue here. Voigt et al. (2013) conducted a random division of the Earth into two halves to assess whether these random pairs exhibited hemispheric symmetry in reflected solar radiation. The results revealed that only 3 % of the random pairs demonstrated a hemispheric difference in reflected radiation smaller than 0.1 W m^{-2}, as measured by CERES-EBAF. Furthermore, even when this criterion was extended tenfold (1 W m^{-2}), only 31% of the random pairs satisfied the hemispheric symmetry requirement. Stephens et al. (2015) noted that the multi-year average hemispheric difference in reflected solar radiation between the NH and SH is less than 0.2 W m^{-2}, suggesting this as an indicator of hemispheric symmetry. Here, when we use a symmetry criterion

https://doi.org/10.5194/egusphere-2023-2882
Preprint. Discussion started: 9 January 2024

of 0.1 W m^{-2}, CERES achieves hemispheric symmetry of reflected radiation on a 16-year annual mean scale, while none of the other datasets do. When we expand this symmetry criterion to 0.2 W m^{-2}, the symmetry study application of CERES is around 9-year scale, and other datasets remain inapplicable. When held to a more conservative standard of 1 W m^{-2}, CERES achieves hemispheric symmetry every year, and AVHRR achieves it on scale of more than two years. Interestingly, the ISCCP exhibits increasing hemispheric asymmetry with longer durations, only declining after a 13-year average. ERA5 also displays a similar but more moderate increase in hemispheric asymmetry. In addition, in order to have a more rigorous standard, we would like to take the uncertainty of the instrumental measurements into account. If the difference between the solar radiation reflected from the NH and SH is within the uncertainty of the measurement, it is considered as hemispherical symmetry (Diamond et al., 2022). The regional averaged monthly mean uncertainty of the reflected SW radiation at the TOA of the CERES EBAF is 2.5 W m^{-2} (Loeb et al., 2018b). AVHRR, ISCCP, MERRA-2 and ERA5 have monthly regional mean biases from the CERES of 3.3 W m^{-2}, 4.8 W m^{-2}, 5.9 W m^{-2} and -1.9 W m^{-2}, respectively, which will be used to calculate their uncertainties. Here we follow the method of Jönsson and Bender (2022) to calculate the uncertainty of hemispheric difference of reflected solar radiation flux, noting that only rough calculations have been made due to the unavailability of uncertainties at different grid points around the globe. Uncertainty in the time-mean over the N-month period is scaled by a factor of $N^{-1/2}$. Then we can obtain a time series of the uncertainty in the hemispherical differences of reflected radiation for each dataset (Fig. S12). It is clear that as time grows, the range of uncertainty shrinks. Note that if the solid black line falls within the shaded area, it indicates that the total reflected radiation exhibits credible hemispheric symmetry within the given uncertainty. The hemispherical difference of the total reflected radiation from CERES remains well within its uncertainty range (not shown). Similarly, AVHRR demonstrates good agreement with uncertainty over a 14-year timescale. On the other hand, ISCCP only maintains this agreement on timescales up to 5 years. The reanalyzed datasets significantly deviate from their respective uncertainty ranges. In summary, AVHRR shows better consistency with CERES regarding the hemispheric symmetry of the total reflected radiation.

Some datasets perform well in total reflected radiation symmetry, it doesn't mean that they also can reasonably simulate the components. Here, we further decompose the TOA total reflected radiation of these datasets into clear- sky atmosphere, surface and cloud components, and compare the performance

https://doi.org/10.5194/egusphere-2023-2882
Preprint. Discussion started: 9 January 2024

of the five datasets on hemispheric differences (Fig. 7). Although AVHRR exhibits well symmetry in the total reflected radiation, it shows considerable deviation from CERES in the hemispherical difference of three components. AVHRR exhibits a brighter SH due to its clear underestimation of the clear-sky atmospheric component contribution in the NH and an overestimation of the cloud component contribution in the SH. Particularly, it significantly overestimates the surface component of the NH. Interestingly, AVHRR even demonstrates a negative correlation (-0.51) with CERES concerning hemispheric differences in the clear-sky atmospheric component, and the data itself displays a high degree of dispersion. This can be attributed, in part, to the limitations of the current AVHRR version regarding aerosols. The aerosol optical thickness is set at 0.05, which is considered an underestimation for high aerosol load situations (Stengel et al., 2020). Furthermore, AVHRR notably overestimates the surface component in the NH. The PVIR mentions that the Cloud_cci dataset exhibits higher biases in TOA upwelling shortwave flux compared to CERES in regions with low vegetation and typically high surface albedo. Additionally, AVHRR demonstrates a significant deviation from CERES in the hemispheric differences of the cloud component. Stengel et al. (2020) highlighted that AVHRR PMv3 shows a greater bias in identifying liquid clouds and reducing ice water paths compared to v2. In terms of ISCCP, the multi-year means of the hemispheric differences for all three components are closest to CERES among the datasets. However, the time series of annual means for the hemispheric difference in the clear-sky atmospheric component and the surface component show poor correlation with CERES. On the other hand, ISCCP performs well in evaluating the hemispheric differences in the cloud component, showing close agreement and a strong correlation with CERES (0.86). Previous studies have indicated that ISCCP employs a visible adjustment to correct for emission through thin cirrus clouds, which enhances the accuracy of cloud top pressure retrievals for single-layer cirrus clouds (Marchand et al., 2010). Additionally, the incorporation of the Max Planck Institute Aerosol Climatology (MAC) in the treatment of stratospheric and tropospheric aerosols within the ISCCP-H series helps reduce the misidentification of aerosols as clouds (Young et al., 2018). However, the aerosol input dataset MAC-v2, despite improving cloud simulation, suffers from significant errors and uncertainties (further details in the 'ISCCP-FH Radiative Flux Profile Product C-ATBD'). This may explain the lack of correspondence between the hemispheric differences in the clear-sky atmospheric components of ISCCP and CERES. Nevertheless, ISCCP still exhibits biases in cloud retrieval. For instance, Boudala and Milbrandt (2021)

https://doi.org/10.5194/egusphere-2023-2882
Preprint. Discussion started: 9 January 2024

discovered that ISCCP data overestimates cloud cover in both hemispheres between approximately 40° and 60° latitude, particularly in North America and Europe, but significantly underestimates cloud cover in the tropics and high latitudes in both hemispheres. Furthermore, ISCCP also overestimates the total cloud fraction of TP compared to other space-based lidars (Zhao et al., 2023). The two reanalysis datasets exhibit different performance in simulating hemispheric differences in the three components. MERRA-2 poorly models the hemispheric difference in the cloud component, whereas ERA5 demonstrates good agreement and correlation with CERES. Hinkelman (2019) pointed out that the discrepancy in all-sky reflected SW radiation flux at TOA between MERRA-2 and EBAF is attributed to differences in cloud variables such as cloud fraction or optical depth. In MERRA-2, there is an excessive presence of clouds over tropical oceans and a slight underestimation of clouds in the oceanic stratocumulus region, as well as an overestimation of clouds in the Southern Ocean (Hinkelman, 2019). It has been shown that MERRA-2 consistently underestimates total cloud cover across almost all areas of the TP at all times (Deng et al., 2023) and altitudes (Zhao et al., 2023). This bias may stem from a flaw in the cloud parameterization within the reanalysis assimilation model (Dolinar et al., 2016; Li et al., 2017). When assessing the cloud properties of reanalysis data over East Asia, Yao et al. (2020) found that ERA5 and MERRA-2 generally overestimate liquid clouds, with MERRA-2 also overestimating ice clouds over the cyclone center. Nevertheless, ERA5 still exhibits good correlation with CERES, except for the hemispheric difference in the clear-sky atmospheric component. Li et al. (2023) demonstrated that the deviation of ERA5's surface solar radiation products from observed values increases with higher aerosol loading, indicating that aerosols have a significant impact on the accuracy of ERA5's radiation products. Furthermore, the cumulative annual mean time series of hemispheric differences in the cloud component for ISCCP and ERA5 display similar variations to CERES, with ISCCP exhibiting a smaller bias. However, the cumulative annual mean time series of hemispheric differences in the surface component for ISCCP differs from all other datasets, as its hemispheric difference increases after the 5-year average but ultimately converges to a constant at longer time scales as others. The cumulative annual mean of hemispheric differences in the clear-sky atmospheric component for AVHRR, ISCCP, and MERRA-2 exhibits similar characteristics to CERES, with a pronounced change, illustrating the irregularity of human activities. In contrast, ERA5 shows a consistent decline.

On the whole, if the focus is solely on studying the hemispheric symmetry of total reflected radiation,

https://doi.org/10.5194/egusphere-2023-2882
Preprint. Discussion started: 9 January 2024

AVHRR can be chosen, although it exhibits poor performance in simulating the hemispheric differences of the components. Conversely, ISCCP can be utilized for studying the hemispheric asymmetry in the cloud component of reflected radiation. Generally, there is scope for improvement in simulating the components of reflected radiation in these datasets. Further research and algorithmic enhancements may be required to address these issues and enhance the usability and accuracy of these datasets in studies related to hemispheric symmetry.

4 Discussion and Summary

The hemispheric symmetry of the PA is a powerful feature of the Earth system, and the mechanisms by which it is currently maintained remain unclear, posing a great challenge for improving the simulation of climate models. Numerous scholars have proposed many possible compensatory mechanisms, and many of the different mechanisms are not only limited by latitude but also have seasonal characteristics, and if we resolve the energy down to monthly scales and latitudinal zones, we can capture more variations in the mechanisms. Accordingly based on the TOA and surface radiative flux data from CERES EBAF during March 2001 to February 2021, we build on the original interannual variability and further explore the contribution and monthly variability of different latitudinal zones as well as the variability of the different components across latitudinal zones, and moreover the manifestation of hemispheric symmetry for the different datasets. The results are as follows:

(1) The total reflected SW radiation at the TOA shows a clear hemispheric symmetry in the long-term trend of the annual and the multi-year average. The annual mean decreasing trend in the NH is synergistically influenced by changes in Arctic snow and ice, reduction in anthropogenic aerosols at mid-latitudes, and a decrease in low cloud cover in the Eastern Pacific. In contrast, the decreasing trend in the SH is mainly due to the cloud component. The cumulative year-to-year averaging of the hemispheric differences in reflected radiation and its components tend to be constant over time, yet the clear-sky atmospheric component displays great variability owing to human activities. More cloud component contribution from 0° N-10° N and more clear-sky atmospheric and surface component contribution from 10° N-60° N compared to the corresponding latitude zones in SH, result in the dominance of NH reflected radiation at 0°-40°. However, greater surface component contribution from higher latitude zones in the SH and significantly higher cloud contribution from 10° S-70° S compensate for this, resulting in the

https://doi.org/10.5194/egusphere-2023-2882
Preprint. Discussion started: 9 January 2024

reflected radiation of SH leading that of the NH in 50°-90°. Within the latitudinal zones from the equator to 40°, the annual cycle of reflected radiation contribution is distinguished by a high in fall/winter and a low in spring/summer, with higher contribution in the NH than in the SH. Nonetheless, beyond 50°, this pattern is reversed entirely. This feature of the annual cycle in various latitudes is linked to that of the incident radiation and is mainly contributed by the cloud and clear-sky atmospheric component at low-mid latitudes, and by the surface component at high latitudes. At high latitudes, the peak of the surface component contribution in the NH is one month earlier than in the SH due to surface albedo and Arctic amplification effects. From the perspective of hemispheric difference, the annual cycle of total reflected radiation and its interannual variability are almost drive from those of cloud component contribution in mid-low latitudes, and from surface and cloud contributions in high latitude zones.

(2) In extreme anomaly years across all latitudinal zones, the primary factor is the cloud component contribution, followed by the surface component, and then the clear-sky atmospheric component. Surface component anomalies play a larger role in extreme events in the SH, particularly in the 60° S-70° S. It is common to observe cancellation of contribution anomalies between different components and latitudinal zones during extreme events. The effect of cloud variability on the variation of reflected radiative contributions of different latitudinal zones is not negligible at both low and high latitudes, for both long-term perturbations and extreme events, and is evidently influenced by large-scale weather patterns such as ENSO and PDO.

(3) According to the DDZJ-DISO assessment system, AVHRR performs best in terms of hemispheric symmetry, followed by ISCCP and ERA5, and the worst is MERRA-2. Under different symmetry criteria (0.1 W m^{-2}, 0.2 W m^{-2}, 1 W m^{-2} and uncertainties of different datasets), the applicability of different datasets to hemispheric symmetry of PA studies varies. AVHRR correlates best with CERES for the time series of hemispheric differences of total reflected radiation, the multi-year mean is closest, and the hemispheric symmetry of the PA can be studied within its uncertainty on 14-year timescale. However, AVHRR does not adequately capture the hemispheric differences of individual components. ERA5 and ISCCP simulate hemispheric differences of total reflected radiation with about the same performance, while ERA5 itself is more stable. If one only wants to study cloud component, consider using ISCCP.

Based on long-term satellite observations, our study and previous research have confirmed a clear

https://doi.org/10.5194/egusphere-2023-2882
Preprint. Discussion started: 9 January 2024

decreasing trend in solar radiation reflected back into space in both hemispheres over the past two decades (Loeb et al., 2020; Stephens et al., 2022). This trend is particularly significant as the increase in net solar energy absorption by the Earth outweighs the increase in outgoing thermal infrared radiation. Consequently, it leads to a rise in global average temperature, exacerbating the Earth's energy imbalance, global warming, sea-level rise, changes in the climate system, and the melting of glaciers and permafrost (Loeb et al., 2021b). Given the profound impact of these changes on the climate system, it is crucial to pay closer attention to the future evolution of PA and its symmetry. Although climate models persistently exhibit biases in simulating the average state of albedo symmetry from CMIP3 to CMIP6 (Crueger et al., 2023), they remain a powerful tool for generating hypotheses about the unexplained observed albedo symmetry (Rugenstein and Hakuba, 2023) and projecting future evolutions and potential influencing mechanisms. For example, Rugenstein and Hakuba (2023) examined the response of modeled surface temperature and PA to CO_2 and found an increasing difference in surface warming between the two hemispheres under stronger carbon dioxide forcing and weaker aerosol forcing. They also proposed that the warmer hemisphere will become darker, suggesting a potential asymmetry in albedo in the coming decades. On the other hand, Diamond et al. (2022) focused on changes in clear-sky hemispheric asymmetry under different emission scenarios simulated by their model. Their results indicated a significant shift in clear-sky albedo asymmetry throughout this century under both high and low emission scenarios, primarily driven by anthropogenic aerosol emissions and cryosphere changes. Furthermore, Jönsson and Bender (2023) investigated the evolution of hemispheric albedo differences following a sudden quadrupling of CO_2 concentration using CMIP6 coupled model simulations. They found that the initial albedo reduction in the NH may be partly compensated by a reduction in extratropical cloudiness in the SH on a much longer timescale which can be referred to as a mechanism of trans-hemispheric communication. They also highlighted that if PA maintains hemispheric symmetry, compensating for cloud variations will have uncertain but significant effects on Earth's energy balance and hydrologic cycle. However, whether the hemispheric symmetry of PA can be sustained indefinitely remains an open question. Therefore, it is essential to focus on investigating additional potential mechanisms of hemispheric albedo symmetry and future projections using model ensembles, along with observational constraints.

https://doi.org/10.5194/egusphere-2023-2882
Preprint. Discussion started: 9 January 2024

Data availability. The CERES_EBAF_Ed4.2 and CERES-SSF1deg products are publicly available through the NASA Langley Research Center CERES ordering tool at https://ceres.larc.nasa.gov/data/. The ESA Cloud-cci version 3 products, AVHRR-PMv3 for this research are included in the paper: Stengel et al. (2020), or obtained through https://public.satproj.klima.dwd.de/data/ESA_Cloud_CCI/CLD_PRODUCTS/v3.0/L3C/. The ISCCP-FH data are available from the following website: https://isccp.giss.nasa.gov/pub/flux-fh/. The MERRA-2 datasets used in this study are available from the following websites: https://doi.org/10.5067/OU3HJDS973O0, https://doi.org/10.5067/OU3HJDS973O0 and https://doi.org/10.5067/FH9A0MLJPC7N. The ERA5 monthly averaged data on single levels from 1940 to present are available from Climate Data Store (CDS) of https://cds.climate.copernicus.eu/cdsapp#!/dataset/reanalysis-era5-single-levels-monthly-means?tab=overview.

Author contributions. RL and BJ organized the paper and performed related analysis. RL drew article graph and prepared the manuscript. BJ and JL conceptualized the paper and revised the whole manuscript. DW and LZ modified the paper and provided suggestions for this study. All authors contributed to the discussion of the results and reviewed the manuscript.

Competing interests. The contact author has declared that none of the authors has any competing interests.

Disclaimer. Publisher's note: Copernicus Publications remains neutral with regard to jurisdictional claims in published maps and institutional affiliations.

Acknowledgements. We would like to thank the CERES, CLOUD_CCI AVHRR, ISCCP, MERRA-2, and ERA5 science teams for providing excellent and accessible data products that made this study possible. We would like to acknowledge the assistance of ChatGPT in proofreading and polishing the language of this manuscript. ChatGPT, an AI language model developed by OpenAI, helped refine the clarity and fluency of the text. We are grateful for its contribution in improving the quality of our work.

Financial support. This research was jointly supported by the National Science Fund for Excellent Young Scholars (42022037), the Major Program of the National Natural Science Foundation of China (42090030), the National Natural Science Foundation of China (42305072), and the China Postdoctoral Science Foundation (2023M731454).

References

Andersen, H., Cermak, J., Zipfel, L., and Myers, T. A.: Attribution of observed recent decrease in low clouds over the Northeastern Pacific to cloud-controlling factors, Geophysical Research Letters, 49, e2021GL096498, https://doi.org/10.1029/2021GL096498, 2022.

Avery, M. A., Davis, S. M., Rosenlof, K. H., Ye, H., and Dessler, A. E.: Large anomalies in lower stratospheric water vapour and ice during the 2015–2016 El Niño, Nature Geoscience, 10, 405-409, https://doi.org/10.1038/NGEO2961, 2017.

Bender, F. A.-M., Rodhe, H., Charlson, R. J., Ekman, A. M., and Loeb, N.: 22 views of the global albedo—comparison between 20 GCMs and two satellites, Tellus A: Dynamic Meteorology and Oceanography, 58, 320-330, https://doi.org/10.1111/j.1600-0870.2006.00181.x, 2006.

Betts, R. A.: Offset of the potential carbon sink from boreal forestation by decreases in surface albedo, Nature, 408, 187-190, https://doi.org/10.1038/35041545, 2000.

Boudala, F. S. and Milbrandt, J. A.: Evaluations of the Climatologies of Three Latest Cloud Satellite Products Based on Passive Sensors (ISCCP-H, Two CERES) against the CALIPSO-GOCCP, Remote Sensing, 13, 5150, https://doi.org/10.3390/rs13245150, 2021.

Budyko, M. I.: The effect of solar radiation variations on the climate of the Earth, tellus, 21, 611-619, https://doi.org/10.3402/tellusa.v21i5.10109, 1969.

Cao, Y., Liang, S., He, T., and Chen, X.: Evaluation of four reanalysis surface albedo data sets in Arctic using a satellite product, IEEE Geoscience and Remote Sensing Letters, 13, 384-388, https://doi.org/10.1109/LGRS.2016.2515159, 2016.

Chen, J. and Dai, A.: The atmosphere has become increasingly unstable during 1979–2020 over the Northern Hemisphere, Geophysical Research Letters, 50, e2023GL106125,

https://doi.org/10.5194/egusphere-2023-2882
Preprint. Discussion started: 9 January 2024

https://doi.org/10.1029/2023GL106125, 2023.

Crueger, T., Schmidt, H., and Stevens, B.: Hemispheric albedo asymmetries across three phases of CMIP, Journal of Climate, 1-34, https://doi.org/10.1175/JCLI-D-22-0923.1, 2023.

Deng, C., Li, J., Li, J., Li, R., Zhang, W., Zhao, Y., Zhao, Y., and Jian, B.: Long-term changes in the diurnal cycle of total cloud cover over the Tibetan Plateau, Atmospheric Research, 106992, https://doi.org/10.1016/j.atmosres.2023.106992 2023.

Diamond, M. S., Gristey, J. J., Kay, J. E., and Feingold, G.: Anthropogenic aerosol and cryosphere changes drive Earth's strong but transient clear-sky hemispheric albedo asymmetry, Commun Earth Environ, 3, 206, https://doi.org/10.1038/s43247-022-00546-y, 2022.

Dolinar, E. K., Dong, X., and Xi, B.: Evaluation and intercomparison of clouds, precipitation, and radiation budgets in recent reanalyses using satellite-surface observations, Climate Dynamics, 46, 2123-2144, https://doi.org/10.1007/s00382-015-2693-z, 2016.

Engström, A., Bender, F. A. M., Wood, R., and Charlson, R. J.: Evaluation of Hemispheric Asymmetries in Marine Cloud Radiative Properties, Journal of Climate, 30, 4131-4147, https://doi.org/10.1175/jcli-d-16-0263.1, 2017.

Fu, Q., Cribb, M., Barker, H., Krueger, S., and Grossman, A.: Cloud geometry effects on atmospheric solar absorption, Journal of the atmospheric sciences, 57, 1156-1168, https://doi.org/10.1175/1520-0469(2000)057<1156:CGEOAS>2.0.CO;2, 2000.

Gelaro, R., McCarty, W., Suárez, M. J., Todling, R., Molod, A., Takacs, L., Randles, C. A., Darmenov, A., Bosilovich, M. G., and Reichle, R.: The modern-era retrospective analysis for research and applications, version 2 (MERRA-2), Journal of climate, 30, 5419-5454, https://doi.org/10.1175/JCLI-D-16-0758.1, 2017.

George, D. and Bjorn, S.: Earth's Albedo and Its Symmetry, AGU Advances, 2, https://doi.org/10.1029/2021AV000440, 2021.

Hadas, O., Datseris, G., Blanco, J., Bony, S., Caballero, R., Stevens, B., and Kaspi, Y.: The role of baroclinic activity in controlling Earth's albedo in the present and future climates, Proceedings of the National Academy of Sciences, 120, e2208778120, https://doi.org/10.1073/pnas.2208778120, 2023.

Hersbach, H., Bell, B., Berrisford, P., Hirahara, S., Horányi, A., Muñoz-Sabater, J., Nicolas, J., Peubey,

https://doi.org/10.5194/egusphere-2023-2882
Preprint. Discussion started: 9 January 2024

C., Radu, R., and Schepers, D.: The ERA5 global reanalysis, Quarterly Journal of the Royal Meteorological Society, 146, 1999-2049, https://doi.org/10.1002/qj.3803, 2020.

Hinkelman, L. M.: The global radiative energy budget in MERRA and MERRA-2: Evaluation with respect to CERES EBAF data, Journal of Climate, 32, 1973-1994, https://doi.org/10.1175/JCLI-D-18-0445.1, 2019.

Hollmann, R., Merchant, C. J., Saunders, R., Downy, C., Buchwitz, M., Cazenave, A., Chuvieco, E., Defourny, P., de Leeuw, G., and Forsberg, R.: The ESA climate change initiative: Satellite data records for essential climate variables, Bulletin of the American Meteorological Society, 94, 1541-1552, https://doi.org/10.1175/BAMS-D-11-00254.1, 2013.

Hu, Y. and Stamnes, K.: An accurate parameterization of the radiative properties of water clouds suitable for use in climate models, Journal of climate, 6, 728-742, https://doi.org/10.1175/1520-0442(1993)006<0728:AAPOTR>2.0.CO;2, 1993.

Hu, Y., Li, D., and Liu, J.: Abrupt seasonal variation of the ITCZ and the Hadley circulation, Geophysical research letters, 34, https://doi.org/10.1029/2007GL030950, 2007, 2007.

Hu, Z.-Z., Kumar, A., Huang, B., Xue, Y., Wang, W., and Jha, B.: Persistent atmospheric and oceanic anomalies in the North Atlantic from summer 2009 to summer 2010, Journal of Climate, 24, 5812-5830, https://doi.org/10.1175/2011JCLI4213.1, 2011.

Hu, Z., Chen, X., Zhou, Q., Chen, D., and Li, J.: DISO: A rethink of Taylor diagram, International Journal of Climatology, 39, 2825-2832, https://doi.org/10.1002/joc.5972, 2019.

Hu, Z., Chen, D., Chen, X., Zhou, Q., Peng, Y., Li, J., and Sang, Y.: CCHZ-DISO: A Timely New Assessment System for Data Quality or Model Performance From Da Dao Zhi Jian, Geophysical Research Letters, 49, e2022GL100681, https://doi.org/10.1029/2022GL100681, 2022.

Huang, B., L'Heureux, M., Hu, Z. Z., and Zhang, H. M.: Ranking the strongest ENSO events while incorporating SST uncertainty, Geophysical Research Letters, 43, 9165-9172, https://doi.org/10.1002/2016GL070888, 2016.

Huang, J.-p., Guan, X.-d., and Ji, F.: Enhanced cold-season warming in semi-arid regions, Atmospheric Chemistry and Physics, 12, 5391-5398, https://doi.org/10.5194/acp-12-5391-2012, 2012.

IPCC, A.: Climate change 2013: the physical science basis, Contribution of working group I to the fifth assessment report of the intergovernmental panel on climate change, 1535, 2013.

https://doi.org/10.5194/egusphere-2023-2882
Preprint. Discussion started: 9 January 2024

Jian, B., Li, J., Wang, G., He, Y., Han, Y., Zhang, M., and Huang, J.: The Impacts of Atmospheric and Surface Parameters on Long-Term Variations in the Planetary Albedo, Journal of Climate, 31, 8705-8718, https://doi.org/10.1175/jcli-d-17-0848.1, 2018.

Jiang, H., Yang, Y., Bai, Y., and Wang, H.: Evaluation of the total, direct, and diffuse solar radiations from the ERA5 reanalysis data in China, IEEE Geoscience and Remote Sensing Letters, 17, 47-51, https://doi.org/10.1109/LGRS.2019.2916410, 2019.

Jiménez-Muñoz, J. C., Mattar, C., Barichivich, J., Santamaría-Artigas, A., Takahashi, K., Malhi, Y., Sobrino, J. A., and Schrier, G. v. d.: Record-breaking warming and extreme drought in the Amazon rainforest during the course of El Niño 2015–2016, Scientific reports, 6, 33130, https://doi.org/10.1038/srep33130, 2016.

Johnson, G. C., Lyman, J. M., and Loeb, N. G.: Improving estimates of Earth's energy imbalance, Nature Climate Change, 6, 639-640, https://doi.org/10.1038/nclimate3043, 2016.

Jönsson, A. and Bender, F. A.-M.: Persistence and variability of Earth’s interhemispheric albedo symmetry in 19 years of CERES EBAF observations, Journal of Climate, 35, 249-268, https://doi.org/10.1175/JCLI-D-20-0970.1, 2022.

Jönsson, A. R. and Bender, F. A.-M.: The implications of maintaining Earth's hemispheric albedo symmetry for shortwave radiative feedbacks, Earth System Dynamics, 14, 345-365, https://doi.org/10.5194/esd-14-345-2023, 2023.

Kalmár, T., Pieczka, I., and Pongrácz, R.: A sensitivity analysis of the different setups of the RegCM4. 5 model for the Carpathian region, International Journal of Climatology, 41, E1180-E1201, https://doi.org/10.1002/joc.6761, 2021.

Kato, S., Loeb, N. G., Rose, F. G., Doelling, D. R., Rutan, D. A., Caldwell, T. E., Yu, L., and Weller, R. A.: Surface irradiances consistent with CERES-derived top-of-atmosphere shortwave and longwave irradiances, Journal of Climate, 26, 2719-2740, https://doi.org/10.1175/JCLI-D-12-00436.1, 2013.

Kato, S., Rose, F. G., Rutan, D. A., Thorsen, T. J., Loeb, N. G., Doelling, D. R., Huang, X., Smith, W. L., Su, W., and Ham, S.-H.: Surface irradiances of edition 4.0 clouds and the earth’s radiant energy system (CERES) energy balanced and filled (EBAF) data product, Journal of Climate, 31, 4501-4527, https://doi.org/10.1175/JCLI-D-17-0523.1, 2018.

Khaykin, S., Legras, B., Bucci, S., Sellitto, P., Isaksen, L., Tencé, F., Bekki, S., Bourassa, A., Rieger, L.,

https://doi.org/10.5194/egusphere-2023-2882
Preprint. Discussion started: 9 January 2024

and Zawada, D.: The 2019/20 Australian wildfires generated a persistent smoke-charged vortex rising up to 35 km altitude, Communications Earth & Environment, 1, 22, https://doi.org/10.1038/s43247-020-00022-5, 2020.

Koplitz, S. N., Mickley, L. J., Marlier, M. E., Buonocore, J. J., Kim, P. S., Liu, T., Sulprizio, M. P., DeFries, R. S., Jacob, D. J., and Schwartz, J.: Public health impacts of the severe haze in Equatorial Asia in September–October 2015: demonstration of a new framework for informing fire management strategies to reduce downwind smoke exposure, Environmental Research Letters, 11, 094023, https://doi.org/10.1088/1748-9326/11/9/094023, 2016.

Letu, H., Nagao, T. M., Nakajima, T. Y., Riedi, J., Ishimoto, H., Baran, A. J., Shang, H., Sekiguchi, M., and Kikuchi, M.: Ice cloud properties from Himawari-8/AHI next-generation geostationary satellite: Capability of the AHI to monitor the DC cloud generation process, IEEE Transactions on Geoscience and Remote Sensing, 57, 3229-3239, https://doi.org/10.1109/TGRS.2018.2882803, 2018.

Letu, H., Ma, R., Nakajima, T. Y., Shi, C., Hashimoto, M., Nagao, T. M., Baran, A. J., Nakajima, T., Xu, J., and Wang, T.: Surface Solar Radiation Compositions Observed from Himawari-8/9 and Fengyun-4 Series, Bulletin of the American Meteorological Society, 104, E1772-E1789, https://doi.org/10.1175/BAMS-D-22-0154.1, 2023.

Li, J., Mao, J., and Wang, F.: Comparative study of five current reanalyses in characterizing total cloud fraction and top-of-the-atmosphere cloud radiative effects over the Asian monsoon region, International Journal of Climatology, 37, 5047-5067, https://doi.org/10.1002/joc.5143, 2017.

Li, J., Lv, Q., Jian, B., Zhang, M., Zhao, C., Fu, Q., Kawamoto, K., and Zhang, H.: The impact of atmospheric stability and wind shear on vertical cloud overlap over the Tibetan Plateau, Atmospheric Chemistry and Physics, 18, 7329-7343, https://doi.org/10.5194/acp-18-7329-2018, 2018.

Li, M., Letu, H., Peng, Y., Ishimoto, H., Lin, Y., Nakajima, T. Y., Baran, A. J., Guo, Z., Lei, Y., and Shi, J.: Investigation of ice cloud modeling capabilities for the irregularly shaped Voronoi ice scattering models in climate simulations, Atmospheric Chemistry and Physics, 22, 4809-4825, https://doi.org/10.5194/acp-22-4809-2022, 2022.

Li, Z.-X. and Le Treut, H.: Cloud-radiation feedbacks in a general circulation model and their dependence

https://doi.org/10.5194/egusphere-2023-2882
Preprint. Discussion started: 9 January 2024

on cloud modelling assumptions, Climate Dynamics, 7, 133-139, https://doi.org/10.1007/BF00211155, 1992.

Li, Z., Yang, X., and Tang, H.: Evaluation of the hourly ERA5 radiation product and its relationship with aerosols over China, Atmospheric Research, 294, 106941, https://doi.org/10.1016/j.atmosres.2023.106941, 2023.

Lim, E.-P. and Hendon, H. H.: Causes and predictability of the negative Indian Ocean Dipole and its impact on La Niña during 2016, Scientific reports, 7, 1-11, https://doi.org/10.1038/s41598-017-12674-z, 2017.

Lim, E.-P., Hendon, H. H., Arblaster, J. M., Chung, C., Moise, A. F., Hope, P., Young, G., and Zhao, M.: Interaction of the recent 50 year SST trend and La Niña 2010: amplification of the Southern Annular Mode and Australian springtime rainfall, Climate dynamics, 47, 2273-2291, https://doi.org/10.1007/s00382-015-2963-9, 2016.

Lim, Y.-K., Kovach, R. M., Pawson, S., and Vernieres, G.: The 2015/16 El Niño event in context of the MERRA-2 reanalysis: A comparison of the tropical Pacific with 1982/83 and 1997/98, Journal of climate, 30, 4819-4842, https://doi.org/10.1175/JCLI-D-16-0800.1, 2017.

Lim, Y.-K., Wu, D. L., Kim, K.-M., and Lee, J. N.: An Investigation on Seasonal and Diurnal Cycles of TOA Shortwave Radiations from DSCOVR/EPIC, CERES, MERRA-2, and ERA5, Remote Sensing, 13, 4595, https://doi.org/10.3390/rs13224595, 2021.

Loeb, N. G., Su, W., Bellouin, N., and Ming, Y.: Changes in clear-sky shortwave aerosol direct radiative effects since 2002, Journal of Geophysical Research: Atmospheres, 126, e2020JD034090, https://doi.org/10.1029/2020JD034090, 2021a.

Loeb, N. G., Wielicki, B. A., Rose, F. G., and Doelling, D. R.: Variability in global top-of-atmosphere shortwave radiation between 2000 and 2005, Geophysical research letters, 34, https://doi.org/10.1029/2006GL028196, 2007.

Loeb, N. G., Thorsen, T. J., Norris, J. R., Wang, H., and Su, W.: Changes in Earth's energy budget during and after the "pause" in global warming: An observational perspective, Climate, 6, 62, https://doi.org/10.3390/cli6030062, 2018a.

Loeb, N. G., Johnson, G. C., Thorsen, T. J., Lyman, J. M., Rose, F. G., and Kato, S.: Satellite and ocean data reveal marked increase in Earth's heating rate, Geophysical Research Letters, 48,

https://doi.org/10.5194/egusphere-2023-2882
Preprint. Discussion started: 9 January 2024

e2021GL093047, https://doi.org/10.1029/2021GL093047, 2021b.

Loeb, N. G., Priestley, K. J., Kratz, D. P., Geier, E. B., Green, R. N., Wielicki, B. A., Hinton, P. O. R., and Nolan, S. K.: Determination of unfiltered radiances from the Clouds and the Earth's Radiant Energy System instrument, Journal of Applied Meteorology, 40, 822-835, https://doi.org/10.1175/1520-0450(2001)040<0822:DOURFT>2.0.CO;2, 2001.

Loeb, N. G., Wielicki, B. A., Doelling, D. R., Smith, G. L., Keyes, D. F., Kato, S., Manalo-Smith, N., and Wong, T.: Toward optimal closure of the Earth's top-of-atmosphere radiation budget, Journal of Climate, 22, 748-766, https://doi.org/10.1175/2008JCLI2637.1, 2009.

Loeb, N. G., Mayer, M., Kato, S., Fasullo, J. T., Zuo, H., Senan, R., Lyman, J. M., Johnson, G. C., and Balmaseda, M.: Evaluating twenty-year trends in Earth's energy flows from observations and reanalyses, Journal of Geophysical Research: Atmospheres, 127, e2022JD036686, https://doi.org/10.1029/2022JD036686, 2022.

Loeb, N. G., Doelling, D. R., Wang, H., Su, W., Nguyen, C., Corbett, J. G., Liang, L., Mitrescu, C., Rose, F. G., and Kato, S.: Clouds and the earth's radiant energy system (CERES) energy balanced and filled (EBAF) top-of-atmosphere (TOA) edition-4.0 data product, Journal of Climate, 31, 895-918, https://doi.org/10.1175/JCLI-D-17-0208.1, 2018b.

Loeb, N. G., Wang, H., Allan, R. P., Andrews, T., Armour, K., Cole, J. N., Dufresne, J. L., Forster, P., Gettelman, A., and Guo, H.: New generation of climate models track recent unprecedented changes in Earth's radiation budget observed by CERES, Geophysical Research Letters, 47, e2019GL086705, https://doi.org/10.1029/2019GL086705, 2020.

Marchand, R., Ackerman, T., Smyth, M., and Rossow, W. B.: A review of cloud top height and optical depth histograms from MISR, ISCCP, and MODIS, Journal of Geophysical Research: Atmospheres, 115, https://doi.org/10.1029/2009JD013422, 2010.

Mika, R., Yu., K. A., Antti, L., Kalle, N., Otto, H., Kimmo, R., Timo, V., and Ari, L.: The Arctic has warmed nearly four times faster than the globe since 1979, Communications Earth & Environment, 3, https://doi.org/10.1038/s43247-022-00498-3, 2022.

Minnis, P., Sun-Mack, S., Chen, Y., Chang, F.-L., Yost, C. R., Smith, W. L., Heck, P. W., Arduini, R. F., Bedka, S. T., and Yi, Y.: CERES MODIS cloud product retrievals for edition 4—Part I: Algorithm changes, IEEE Transactions on Geoscience and Remote Sensing, 59, 2744-2780,

https://doi.org/10.5194/egusphere-2023-2882
Preprint. Discussion started: 9 January 2024

https://doi.org/10.1109/TGRS.2020.3008866, 2020.

Noël, B., Van De Berg, W., Van Meijgaard, E., Kuipers Munneke, P., Van De Wal, R., and Van Den Broeke, M.: Evaluation of the updated regional climate model RACMO2. 3: summer snowfall impact on the Greenland Ice Sheet, The Cryosphere, 9, 1831-1844, https://doi.org/10.5194/tc-9-1831-2015, 2015.

North, G. R., Cahalan, R. F., and Coakley Jr, J. A.: Energy balance climate models, Reviews of Geophysics, 19, 91-121, https://doi.org/10.1029/RG019i001p00091, 1981.

Pang, G., Chen, D., Wang, X., and Lai, H.-W.: Spatiotemporal variations of land surface albedo and associated influencing factors on the Tibetan Plateau, Science of the Total Environment, 804, 150100, https://doi.org/10.1016/j.scitotenv.2021.150100, 2022.

Qu, X. and Hall, A.: Surface contribution to planetary albedo variability in cryosphere regions, Journal of Climate, 18, 5239-5252, https://doi.org/10.1175/JCLI3555.1, 2005.

Quaas, J., Jia, H., Smith, C., Albright, A. L., Aas, W., Bellouin, N., Boucher, O., Doutriaux-Boucher, M., Forster, P. M., and Grosvenor, D.: Robust evidence for reversal of the trend in aerosol effective climate forcing, Atmospheric Chemistry and Physics, 22, 12221-12239, https://doi.org/10.5194/acp-22-12221-2022, 2022.

Raghuraman, S. P., Paynter, D., and Ramaswamy, V.: Anthropogenic forcing and response yield observed positive trend in Earth's energy imbalance, Nature communications, 12, 4577, https://doi.org/10.1038/s41467-021-24544-4, 2021.

Riihelä, A., Bright, R. M., and Anttila, K.: Recent strengthening of snow and ice albedo feedback driven by Antarctic sea-ice loss, Nature Geoscience, 14, 832-836, https://doi.org/10.1038/s41561-021-00841-x, 2021.

Rugenstein, M. and Hakuba, M.: Connecting hemispheric asymmetries of planetary albedo and surface temperature, Geophysical Research Letters, 50, e2022GL101802, https://doi.org/10.1029/2022GL101802, 2023.

Saavedra, F. A., Kampf, S. K., Fassnacht, S. R., and Sibold, J. S.: A snow climatology of the Andes Mountains from MODIS snow cover data, International Journal of Climatology, 37, 1526-1539, https://doi.org/10.1002/joc.4795, 2017.

Sandholt, I., Rasmussen, K., and Andersen, J.: A simple interpretation of the surface

https://doi.org/10.5194/egusphere-2023-2882
Preprint. Discussion started: 9 January 2024

temperature/vegetation index space for assessment of surface moisture status, Remote Sensing of environment, 79, 213-224, https://doi.org/10.1016/S0034-4257(01)00274-7, 2002.

Schiffer, R. A. and Rossow, W. B.: The International Satellite Cloud Climatology Project (ISCCP): The first project of the world climate research programme, Bulletin of the American Meteorological Society, 64, 779-784, https://doi.org/10.1175/1520-0477-64.7.779, 1983.

Schmeisser, L., Hinkelman, L. M., and Ackerman, T. P.: Evaluation of radiation and clouds from five reanalysis products in the northeast Pacific Ocean, Journal of Geophysical Research: Atmospheres, 123, 7238-7253, https://doi.org/10.1029/2018JD028805, 2018.

Seinfeld, J. H., Bretherton, C., Carslaw, K. S., Coe, H., DeMott, P. J., Dunlea, E. J., Feingold, G., Ghan, S., Guenther, A. B., and Kahn, R.: Improving our fundamental understanding of the role of aerosol−cloud interactions in the climate system, Proceedings of the National Academy of Sciences, 113, 5781-5790, https://doi.org/10.1073/pnas.1514043113, 2016.

Shikwambana, L., Xongo, K., Mashalane, M., and Mhangara, P.: Climatic and Vegetation Response Patterns over South Africa during the 2010/2011 and 2015/2016 Strong ENSO Phases, Atmosphere, 14, 416, https://doi.org/10.3390/atmos14020416, 2023.

Stengel, M., Stapelberg, S., Sus, O., Finkensieper, S., Würzler, B., Philipp, D., Hollmann, R., Poulsen, C., Christensen, M., and McGarragh, G.: Cloud_cci Advanced Very High Resolution Radiometer post meridiem (AVHRR-PM) dataset version 3: 35-year climatology of global cloud and radiation properties, Earth System Science Data, 12, 41-60, https://doi.org/10.5194/essd-12-41-2020, 2020.

Stephens, G. L., O'Brien, D., Webster, P. J., Pilewski, P., Kato, S., and Li, J.-l.: The albedo of Earth, Reviews of Geophysics, 53, 141-163, https://doi.org/10.1002/2014rg000449, 2015.

Stephens, G. L., Hakuba, M. Z., Kato, S., Gettelman, A., Dufresne, J.-L., Andrews, T., Cole, J. N., Willen, U., and Mauritsen, T.: The changing nature of Earth's reflected sunlight, Proceedings of the Royal Society A, 478, 20220053, https://doi.org/10.1098/rspa.2022.0053, 2022.

Su, W., Corbett, J., Eitzen, Z., and Liang, L.: Next-generation angular distribution models for top-of-atmosphere radiative flux calculation from CERES instruments: Methodology, Atmospheric Measurement Techniques, 8, 611-632, https://doi.org/10.5194/amt-8-611-2015, 2015.

Sus, O., Stengel, M., Stapelberg, S., McGarragh, G., Poulsen, C., Povey, A. C., Schlundt, C., Thomas, G., Christensen, M., and Proud, S.: The Community Cloud retrieval for CLimate (CC4CL)–Part 1:<?

https://doi.org/10.5194/egusphere-2023-2882
Preprint. Discussion started: 9 January 2024

xmltex\break?> A framework applied to multiple satellite imaging sensors, Atmospheric Measurement Techniques, 11, 3373-3396, https://doi.org/10.5194/amt-11-3373-2018, 2018.

Verlinden, K. L., Thompson, D. W., and Stephens, G. L.: The three-dimensional distribution of clouds over the Southern Hemisphere high latitudes, Journal of Climate, 24, 5799-5811, https://doi.org/10.1175/2011JCLI3922.1, 2011.

Voigt, A., Stevens, B., Bader, J., and Mauritsen, T.: The observed hemispheric symmetry in reflected shortwave irradiance, Journal of Climate, 26, 468-477, https://doi.org/10.1175/JCLI-D-12-00132.1, 2013.

Voigt, A., Stevens, B., Bader, J., and Mauritsen, T.: Compensation of hemispheric albedo asymmetries by shifts of the ITCZ and tropical clouds, Journal of Climate, 27, 1029-1045, https://doi.org/10.1175/JCLI-D-13-00205.1, 2014.

Von Schuckmann, K., Palmer, M., Trenberth, K. E., Cazenave, A., Chambers, D., Champollion, N., Hansen, J., Josey, S., Loeb, N., and Mathieu, P.-P.: An imperative to monitor Earth's energy imbalance, Nature Climate Change, 6, 138-144, https://doi.org/10.1038/NCLIMATE2876, 2016.

Wang, G. and Cai, W.: Two-year consecutive concurrences of positive Indian Ocean Dipole and Central Pacific El Niño preconditioned the 2019/2020 Australian “black summer” bushfires, Geoscience Letters, 7, 1-9, https://doi.org/10.1186/s40562-020-00168-2, 2020.

Wang, Y., Huang, X., Liang, H., Sun, Y., Feng, Q., and Liang, T.: Tracking snow variations in the Northern Hemisphere using multi-source remote sensing data (2000–2015), Remote Sensing, 10, 136, https://doi.org/10.3390/rs10010136, 2018.

Wang, Y., Wang, M., Zhang, R., Ghan, S. J., Lin, Y., Hu, J., Pan, B., Levy, M., Jiang, J. H., and Molina, M. J.: Assessing the effects of anthropogenic aerosols on Pacific storm track using a multiscale global climate model, Proceedings of the National Academy of Sciences, 111, 6894-6899, https://doi.org/10.1073/pnas.1403364111, 2014.

Wielicki, B. A., Barkstrom, B. R., Harrison, E. F., Lee III, R. B., Smith, G. L., and Cooper, J. E.: Clouds and the Earth's Radiant Energy System (CERES): An earth observing system experiment, Bulletin of the American Meteorological Society, 77, 853-868, https://doi.org/10.1175/1520-0477(1996)077<0853:CATERE>2.0.CO;2, 1996.

Wielicki, B. A., Wong, T., Loeb, N., Minnis, P., Priestley, K., and Kandel, R.: Changes in Earth's albedo

https://doi.org/10.5194/egusphere-2023-2882
Preprint. Discussion started: 9 January 2024

measured by satellite, Science, 308, 825-825, https://doi.org/10.1126/science.1106484, 2005.

Xiao, Y., Ke, C.-Q., Shen, X., Cai, Y., and Li, H.: What drives the decrease of glacier surface albedo in High Mountain Asia in the past two decades?, Science of The Total Environment, 863, 160945, https://doi.org/10.1016/j.scitotenv.2022.160945, 2023.

Yang, Y., Zhao, C., and Fan, H.: Spatiotemporal distributions of cloud properties over China based on Himawari-8 advanced Himawari imager data, Atmospheric Research, 240, 104927, https://doi.org/10.1016/j.atmosres.2020.104927, 2020.

Yao, B., Liu, C., Yin, Y., Liu, Z., Shi, C., Iwabuchi, H., and Weng, F.: Evaluation of cloud properties from reanalyses over East Asia with a radiance-based approach, Atmospheric Measurement Techniques, 13, 1033-1049, https://doi.org/10.5194/amt-13-1033-2020, 2020.

Young, A. H., Knapp, K. R., Inamdar, A., Hankins, W., and Rossow, W. B.: The international satellite cloud climatology project H-Series climate data record product, Earth System Science Data, 10, 583-593, https://doi.org/10.5194/essd-10-583-2018, 2018.

Zhang, Y., Rossow, W. B., Lacis, A. A., and Oinas, V.: Calculation, evaluation and application of long-term, global radiative flux Datasets at ISCCP: Past and present, in: Studies of Cloud, Convection and Precipitation Processes Using Satellite Observations, World Scientific, 151-177, https://doi.org/10.1142/9789811256912_0009, 2023.

Zhao, C., Chen, Y., Li, J., Letu, H., Su, Y., Chen, T., and Wu, X.: Fifteen-year statistical analysis of cloud characteristics over China using Terra and Aqua Moderate Resolution Imaging Spectroradiometer observations, International Journal of Climatology, 39, 2612-2629, https://doi.org/10.1002/joc.5975, 2019.

Zhao, Y., Li, J., Zhang, L., Deng, C., Li, Y., Jian, B., and Huang, J.: Diurnal cycles of cloud cover and its vertical distribution over the Tibetan Plateau revealed by satellite observations, reanalysis datasets, and CMIP6 outputs, Atmospheric Chemistry and Physics, 23, 743-769, https://doi.org/10.5194/acp-23-743-2023, 2023.

Zhao, Y., Zhao, Y., Li, J., Wang, Y., Jian, B., Zhang, M., and Huang, J.: Evaluating cloud radiative effect from CMIP6 and two satellite datasets over the Tibetan Plateau based on CERES observation, Climate Dynamics, 1-20, https://doi.org/10.1007/s00382-021-05991-7, 2022.

Zhou, Q., Chen, D., Hu, Z., and Chen, X.: Decompositions of Taylor diagram and DISO performance

https://doi.org/10.5194/egusphere-2023-2882
Preprint. Discussion started: 9 January 2024

criteria, International Journal of Climatology, 41, 5726-5732, https://doi.org/10.1002/joc.7149, 2021.